

https://dspace.org/

The use of time-lapse electrical resistivity tomography to determine the footprint of acid mine drainage on groundwater

Zulu, Sbonelo Mfezeko

2017

http://hdl.handle.net/10539/23591

Zulu, Sbonelo Mfezeko (2017) The use of time-lapse electrical resistivity tomography to determine the footprint of acid mine drainage on groundwater, University of the Witwatersrand, Johannesburg, <http://hdl.handle.net/10539/23591>

Downloaded from a DSpace repository. https://dspace.org/

The use of time-lapse electrical resistivity tomography to determine the footprint of acid mine drainage on groundwater

Sbonelo Mfezeko Zulu

Student number: 1272678

GEOL 7028 – Research Report



WITS
UNIVERSITY

For partial fulfillment of the Master of Science in Hydrogeology

5 June 2017

School of Geosciences

University of the Witwatersrand

Supervisor: Dr. Musa Manzi

Co -supervisor: Dr. Michael van Schoor

I declare that this research is my own, independent work. This research report is being submitted in partial fulfilment of the requirements for the degree, Master of Sciences (coursework and research) in Hydrogeology at the University of the Witwatersrand, Johannesburg. It has not been submitted for degree awarding or examination purposes at any other university.

_____

(Signature)

Sbonelo Mfezeko Zulu; BSc (Hons),

Cert.Nat.Sci (No: 200126/12)

ACKNOWLEDGEMENTS

I would like to thank the CSIR for affording me the opportunity and time to pursue my MSc study.

I would also like to sincerely thank my supervisors Dr. Michael van Schoor and Dr. Musa Manzi for the guidance and support throughout the study. I would also like to thank Bongi Maposa for the mentoring during the course of the study.

My mother, Mrs. Duduzile Zulu for her undying support for everything I do, my siblings, Lwandile Zulu and Londeka Maphanga for the motivation when all hope was lost. Last but not least, the crew (Nieces and Nephews).

Dedicated to the memory of my sister:

Nokuzola Hlengiwe Zulu

1974 - 2012

Abstract

The costs of acid mine drainage (AMD) monitoring result in the quest for alternative non-invasive method that can provide qualitative data on the progression of the pollution plume and ground geophysics was the ideal solution. However, the monitoring of AMD plume progression by ground geophysics (time-lapse electrical resistance) proves to be non-invasive but also time consuming.

This study focuses on the modeling of different geophysical anomalies (mainly geoelectrical resistivity response) of the karstic aquifers. The models are generated from field parameters such as the electrical resistivity of the host rock and the target rock, depth to the target, noise level and electrode configuration in order to ensure that the model outcomes represent the actual field data. This process uses Complex Resistivity Model (CRMod) and Complex Resistivity Tomography (CRTomo) to generate geoelectric subsurface models. Different resistivity values are applied to targets in order to assess the difference against the baseline model for each target scenario. The resistivity difference is reduced to smallest possible value between the reference and new models in order to gauge the lowest percentage change in the model at which the background noises start to have impact on the results.

The study shows that the behavior of targets (aquifer) could be clearly detected through resistivity difference tomography rather than inversion tomography. The electrode array plays a significant part in the detection of target areas and their differences in resistance because of its sensitivity. This therefore indicates that the electrode array should be chosen according to study requirements. Furthermore, this study shows that the modelling of different target sizes, alignments and shapes plays huge role in the final results. Future studies that can provide a correlation between the field quantitative data from sampling and the model outcomes have the ability to add to the knowledge of geophysical modeling, thus reducing costs associated with field based plume AMD monitoring.

Key words: Acid mine drainage, geophysics, karst aquifer, complex resistance, modelling, tomography

Table of Contents

1. INTRODUCTION 1
1.1. The problem of AMD in the COH WHS 2
1.2. Research problem 3
1.3. Research motivation 3
1.4. Research questions 4
1.5. Research Aims and objectives 4
Aim 4
Objectives 4
1.6. Envisaged outcomes of the study 5
2. STUDY AREA 6
2.1. Location 6
2.2. Regional geology 7
2.2.1 Stratigraphy of the COH WHS 8
2.3. Water resources of the COH WHS 12
2.3.1 Hydrology 12
2.3.2 Hydrochemistry 14
2.3.3 Karstic aquifers 15
2.4. AMD process 17
2.5. Other study area factors 20
3. ELECTRICAL RESISTIVITY BACKGROUND 21
3.1 Basics of electrical resistivity 22
3.2 Electrode configurations used in electrical resistance surveys 25
3.3 Electrical resistivity tomography 28
3.3.1 The forward model theory 31
3.3.2 Inversion theory 32
4. METHODOLOGY 34
4.1. Background 34
4.2. Forward modelling using the CRMod 34
4.3. Inversion using CRTomo 35
4.4. Image appraisal 37
4.5. Computer simulations 37
5. MODEL STUDY 41
5.1. Study approach 41

5.2. Baseline geoelectric models 41
5.3. Model change specifications 43
5.4. Results 43
5.5. Discussion 66
6. CONCLUSION AND RECOMMENDATION 68
6.1. Conclusion 68
6.2. Recommendation 69

List of figures

Figure 1: Location of the COH WHS 6
Figure 2: Geological map of Johannesburg Dome and surrounding lithology source……...8
Figure 3: Lithostratigraphy of COH WHS..... .11
Figure 4: Compartments within the COH WHS and the groundwater flow direction.……13
Figure 5: Groundwater movement and Sulphates concentration within the study area..... 17
Figure 6: Pre and Post 2014 water quality..... 19
Figure 7: Resistivity scale 22
Figure 8: Current (A, B), potential (M,N) electrodes and equipotentials..... 23
Figure 9: Electrical resistance arrays and their uses 26
Figure 10: Typical sounding technique representation 29
Figure 11: Electrode arrangement for a 2D Electrical survey..... 30
Figure 12: Typical 2D ERT output image..... 30
Figure 13: Individual cells from RES2DMOD..... 31
Figure 14: Different electrode array sensitivity 37
Figure 15: Mesh with electrodes 39
Figure 16: Baseline models..... 42
Figure 17: Model 1 inversion models..... 44
Figure 18: Inversion images with relative limits 46
Figure 19: Model 1 difference images 48
Figure 20: Model 2 inversion images with actual limits..... 49
Figure 21: Inversion images with same resistance limits..... 50
Figure 22: Model 2 difference images 51
Figure 23: Model 3 inversion images..... 53
Figure 24: Model 3 difference images 54
Figure 25: Model 4 inversion images..... 56
Figure 26: Model 4 difference images 57
Figure 27: Model 5 inversion images..... 59
Figure 28: Model 5 difference images 60
Figure 29: Model 6 inversion images..... 61
Figure 30: Model 6 difference images 62
Figure 31: Model 7 inversion images..... 64
Figure 32: Model 7 difference images 65

List of tables

Table 1: Model change specifications 43

LIST OF ABBREVIATIONS

Symbols or abbreviations	**Explanation**
Al	Aluminium
Mn	Manganese
Cl	Chlorine
SO_4	Sulphate
Fe	Iron
Mg	Magnesium
HCO_3^-	Bicarbonate
Ca	Calcium
H_2SO_4	Sulphuric acid
OH	Hydroxide
H_2O	Water
CSIR	Council for Scientific and Industrial Research
WWTW	Waste Water Treatment Works
ERT	Electrical Resistance Tomography
COH WHS	Cradle of Humankind World Heritage Site
AMD	Acid Mine Drainage
WRC	Water Research Council
Mℓ/d	Mega litres per day
CRMod2D	Complex Resistance Model
CRTomo	Complex Resistance Tomography
CRMod	Complex Resistance Model

1. INTRODUCTION

Acid mine drainage (AMD) is a well-documented water resources challenge in the Cradle of Humankind World Heritage Site (COH WHS). This challenge results from the decommissioned mines that decant poor quality water with high sulphate content into the receiving streams that eventually end up in the dolomitic aquifer of the study area. A mine water treatment facility to reduce AMD has been installed but due to heavy rains, its treating capacity has been exceeded which has resulted in treated, semi-treated and raw mine water being decanted into the receiving streams. The impact of mine water on water resources has detrimental effects on the ecosystem as well as on groundwater users within the COH WHS, especially the Zwartkrans Compartment. The karst aquifer within the Zwartkrans compartment in COH WHS experiences pollution at higher rates than primary aquifers since it consists of cavities, unlike the primary aquifers where water infiltrates at slow and steady rates (Daher et al., 2011; Robins et al., 2007). The receiving parts of the study area experience high levels of heavy metals and salts which are produced by the effluent from the decanting mines that are located closer to the Zwartkrans compartment. Historical records indicate that the decline in water quality reached the pH of 3.0 and the conductivity of 550 mS/m (Robins et al., 2007). Deteriorating water quality within the study area was first observed in 2002 and several AMD monitoring methods on water resources have been in place since 2010 (Hobbs et al., 2011).

The establishment of monitoring systems for both ground and surface water within the COH WHS focused on assessing the extent of the contamination footprint, which covers an area of approximately 20 km^2 of the karst aquifer that underlies the Zwartkrans compartment. Boreholes have been used to monitor the quality and the fluctuation of groundwater within the Zwartkrans compartment.

Since the costs for monitoring the aquifer are high, the Water Research Commission (WRC) is conducting a study that seeks to find suitable alternative methods such as surface geophysics to obtain similar information at a reduced cost. This geophysics-based study thus forms part of the Water Research Commission (WRC) project, which is currently being conducted by the Council for Scientific and Industrial Research (CSIR). The study includes several baseline electrical resistance tomography (ERT) surveys at selected sites within the AMD-affected area. The aim of the WRC project was to investigate the use of time-lapse geophysical imaging in identifying changes in the subsurface resistance structure, which could potentially be correlated with changes in the acidity of the aquifer.

1.1. The problem of AMD in the COH WHS

The gold mining industry has contributed significantly over time to the economic growth of South Africa. However, devastating results of AMD emanate from the reaction of the newly exposed rock with water and the atmosphere. The newly exposed rock reacts with the environment which results in the formation of sulphates that become toxic to the water resources and the ecosystem (Durand, 2012). This process is aggravated where the mines are abandoned because there are no groundwater draining measures in place. AMD is rarely experienced in places where mining operations are still on-going because the flow of groundwater is controlled by constant pumping.

The AMD process is influenced by factors such as temperature, available water and microorganisms. However, this is not the case in places where operations have been abandoned (Simate and Ndlovu, 2014). This is because contaminated water infiltrates the soil as the groundwater table returns to its pre-mining state and inevitably contaminates near-surface groundwater. Minerals in rocks oxidise and become unstable upon exposure to water and oxygen. Evaporation and microorganisms also enhance the process which results in more dissolved constituents, therefore generating highly acidic water (Simate and Ndlovu, 2014; Nordstrom et al., 2015). Oxidation of sulphides such as pyrite is generally responsible for most of the AMD.

The impact of AMD

In dolomite, the rock-water interaction triggers a series of reaction between the rock and acid water. The reaction results in the dissolution of carbonate rock thereby causing more cavities within the karst environment (Klimchouk, 2009). The prolonged rock-water interaction causes the dissolution of the carbonate minerals within the dolomitic rock which results in cavities that store water. The process is demonstrated in the equation below:

$$CaMg(CO_3)_2 + 2H_2O + 2CO_2 \rightarrow Ca^{2+} + Mg^{2+} + 4HCO_3$$

Furthermore, the precipitation of sulphates in water results in slower reaction processes which eventually cause AMD to infiltrate much further into the aquifer and away from the pollution source because of the reduced buffering capacity of carbonate minerals within the aquifer by acid mine water (Hobbs et al., 2011; Oberholster et al., 2013).

1.2. Research problem

The Department of Water and Sanitation (DWS), Mogale City Local Municipality (MCLM) and neighbouring mines have taken measures to monitor the degree of groundwater contamination. Groundwater monitoring through sample collection from strategically located points within the Zwartkrans compartment provides absolute quantitative water quality data of the contamination footprint. However, this approach is labour intensive, time consuming and costly (Aizebeokhai and Oyeyemi, 2014). A ground geophysical method could potentially provide a more cost effective alternative to obtaining subsurface data regarding the pseudo-plume.

There are a number of geophysical methods that are applicable to the study of groundwater contamination, and a high-resolution geophysical survey method such as time-lapse electrical resistance tomography has the potential to improve the depiction of the contamination footprint and further monitor its possibly migrating boundaries.

As part of a broader geophysical project in the area, this study focuses on the applicability of time-lapse or difference ERT. This concept is studied by means of numerical modelling. The aim of the model study is to gauge the sensitivity of the time-lapse approach and to predict how effective it might be at detecting and quantifying subtle changes in groundwater salinity that are associated with changes in pollution intensity.

1.3. Research motivation

As much as the boreholes and other aquifer monitoring methods are effective, cost implications may require a supplementary approach towards aquifer monitoring for pollution. This is because it is not financially feasible to drill boreholes on a closely spaced grid across the whole of the Zwartkrans compartment of the COH WHS area to assess the level of groundwater pollution, hence the strategic location of boreholes.

Time-lapse electrical resistance tomography is one of the popular and growing geophysical methods that can be used to supplement available borehole-based data collection methods by monitoring changes in the aquifer's electrical response in the presence or absence of boreholes (Johnson et al., 2012). ERT is sensitive to a variety of parameters including

porosity, the chemistry of the pore fluid, clay content, and the degree of weathering, to name a few. Therefore, by repeating ERT surveys over a period of time one may be able to detect the changes in groundwater salinity over time.

The numerical modelling or computer simulation of scenarios has a potential to determine if the proposed field survey approach of time-lapse ERT will yield the required results or not. Such an approach may help limit the use of geophysical surveys by mimicking the actual field conditions. In doing so, the performance of the proposed geophysical approach can be predicted and survey parameters can also be optimised for future surveys.

1.4. Research questions

This study thus aims to answer the questions:

- Can time-lapse ERT identify the change in aquifer resistance as the pollution intensity changes over time?
- How sensitive is the time-lapse approach to small changes in pollution levels?

1.5. Research Aims and objectives

Aim

The aim of the study was to simulate changing groundwater quality using high-resolution ground geophysics through forward modelling (simulation) of realistic scenarios and subsequent inverse modelling of the associated synthetic responses.

Objectives

- Define simple, but realistic, geoelectric models that can represent typical scenarios from the study area.
- Implement subtle perturbations that simulate changes that might be attributable to changes in pollution levels over a given period.
- Conduct time-lapse ERT modelling to determine whether this approach can detect the above model perturbations.

- Run a series of simulations for different scenarios to benchmark the sensitivity and applicability of the time-lapse approach.

1.6. Envisaged outcomes of the study

The proposed study will improve the current and future contaminant concentration monitoring methods in a karst environment. This will be advantageous in the following ways:

- Clearer depiction of the contamination footprint will help contribute to more effective measures of AMD monitoring and possibly for monitoring remediation of the aquifer.
- If the study indicates that the time-lapse approach is viable it would enable the generation and comparison of data on an on-going basis, which will improve our understanding of the dynamic nature of the contaminants.

2. STUDY AREA

2.1. Location

The COH WHS area is located about 75 km southwest of Pretoria, north of Krugersdorp town on the border of Gauteng and the Northwest province (Figure 1). The key features within the study area are the Sterkfontein Caves and abandoned mines. This study focuses on the COH WHS where the pollution of groundwater by AMD is at its highest. The surrounding communities are dependent on groundwater for domestic use and farming activities.

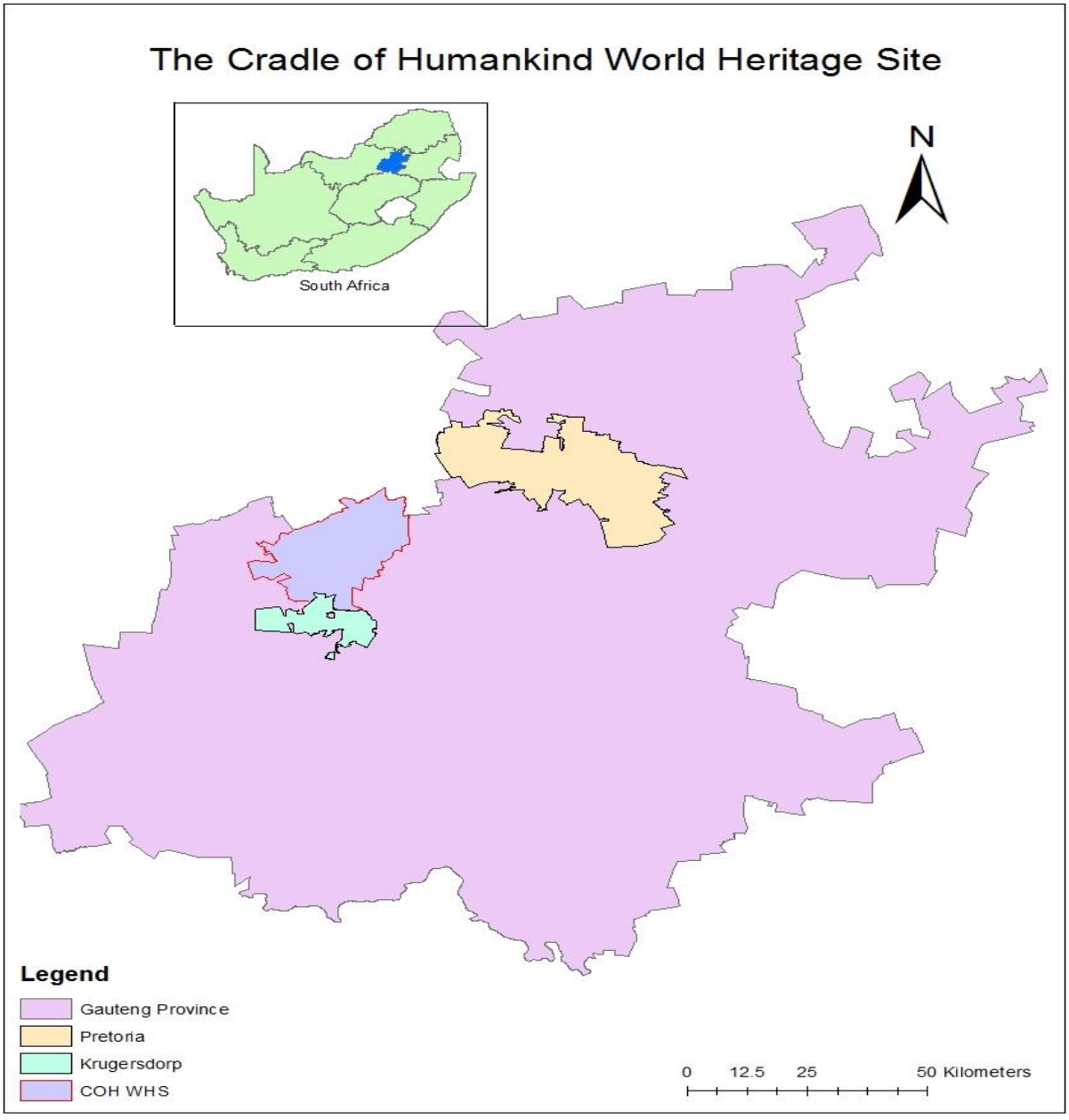

Figure 1: The map of South Africa (top left) shows the Gauteng province where the study area is located while the main map shows the actual location of the study area (COH WHS) localities the Krugersdorp and Pretoria cities(modified from Hobbs, 2015).

Private borehole owners are more prone to consuming contaminated water since it is consumed directly from the aquifer with minimal or no form of treatment.

2.2. Regional geology

The study area lies on four geological supergroups namely the Swaziland (3.1 Ga), Witwatersrand (2.71 Ga), Ventersdorp (2.71 Ga), Transvaal (2.15 Ga) and Karoo Supergroup (0.28 Ga) referred to in Figure 2 below. The Transvaal Supergroup dominates the area and the other three are not dominant in the study area. The Transvaal Supergroup is made up of the two groups which are the Chuniespoort Group and Pretoria Group. The dolomitic strata of the Malmani Subgroup (2.4 Ga) under the Chuniespoort Group dominate the study area and are followed by chert breccia of the Pretoria Group (2.15 Ga) which borders the study area from the West to the North-eastern side of the study area. Shale strata of the Pretoria Group are the third most dominant strata within the study area (Dirks et al., 2016). The ultramafic intrusions and TT gneiss (3.3 Ga) of the Swaziland Supergroup borders the southwestern part of the study area along with a minor portion of andesite of the Ventersdorp Supergroup. A small portion of shale units from the Witwatersrand Supergroup forms part of the south and eastern parts of the study area (Figure 2).

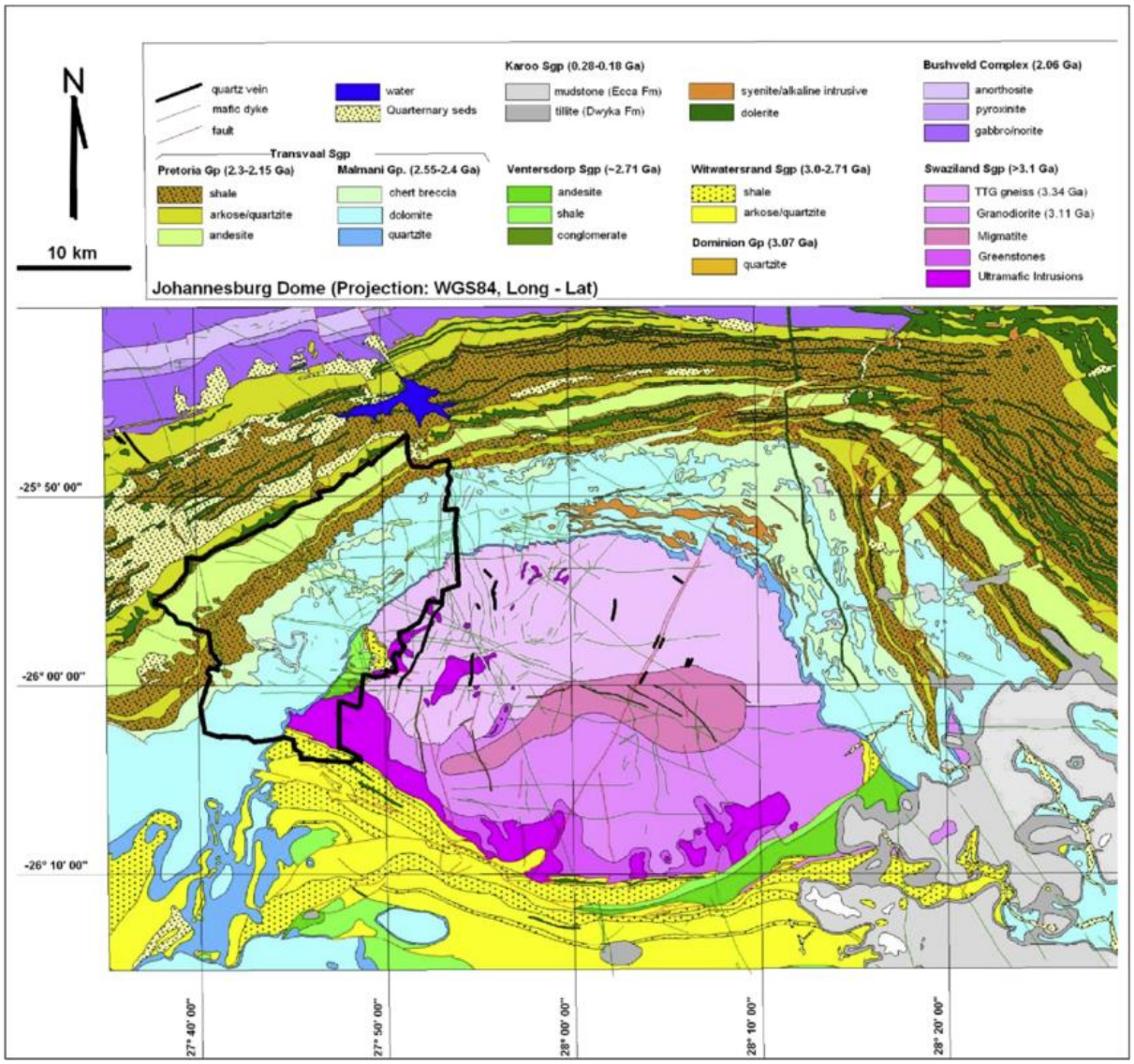

Figure 2: Geological map that shows geological groups that fall within the study (outlined in black) area (Dirks et al., 2016).

2.2.1 Stratigraphy of the COH WHS

The Witwatersrand Supergroup is adjacent to the study area and consists of the Upper Central Rand Group which is dominated by a 2.8 km thick quartz-pyrite, sandstone, shale and a minor amount of conglomerates.

The Upper Central Rand Group is subdivided into the Turffontein and Johannesburg Subgroups. The 3 km thick Central Rand Group overlies the 5 km thick lower West Rand Group which is further divided into three formations, namely, Hospital Hill, Government and Jeppestown Subgroups. The Jeppestown and Government Subgroups are made up of

immature sandstone, conglomerates, siltstone carbonaceous shale, magnetic and nonmagnetic mudstones. The Hospital Hill consists of magnetic mudstone, mature quartz, carbonaceous mudstone and siltstone shale as well as a banded iron formation which consists of offshore sediments such as silt stone-shale, sandstone and mudstone (Guy et al., 2012; Agangi et al., 2015; Fuchs et al., 2015; Viehmann et al., 2015).

The Witwatersrand Supergroup is overlaid by the Transvaal Supergroup which consists of Protobasinal rocks that are made up of a formation with the age that varies from 2714 Ma to 2658 Ma. These formations include Buffelfontein, Tswene-Tshwene, Godwan, Wilkerberg, Wachteenbeetjie, Bloompoort and Mogobane Formation.

The Black Reef formation (2658 Ma – 2550 Ma), which overlies the Protobasinal rock, contains incised valley fill, braided fluvial, shallow marine and braid delta. The Chuniespoort Group (2550 Ma – 2400 Ma), which contains the Malmani Subgroup, overlies the Black Reef Formation. The older formations within the Chuniespoort Group that fall under the Malmani Subgroup are the Oaktree, Monte Christo, Lyttelton, Eccles, and Frisco Formations (Figure 3).

The Oaktree Formation is a chert-poor dolomite formation that forms the base of the Malmani Subgroup. This formation overlies the conglomerate and quartzites of the Black Reef Formation. It is also interbedded within carbonaceous shale horizons. In addition, the upper end of this formation contains columnar and dome stromatolites that are interbedded with carbonaceous mudstones and quartzenites (Dirks and Berger, 2013; Dirks et al., 2016).

The Monte Christo Formation contains a chert-rich dolomite formation with thicknesses of up to 700 m and it is interbedded with shale horizons with thicknesses of less than 50 cm. The base of this formation is dominated by oolites while the top of the formation has 5 m thick layer of chert breccia (Dirks and Berger, 2013).

The Lyttelton Formation (shown Figure 3) consists of a well bedded chert-free dolomite with large stromatolites that are overlain by deformed layers of chert breccia and dolomite horizon. The base of the formation contains Blyde River quartzite which is divided into an interbedded upper ripple laminated quartzite and lower planar laminated carbonaceous mudstone. The middle section of the formation consists of a minor quartzite zone and is dominated by carbonaceous mudstone, columnar stromatolite and ripple laminated grain stone (Dirks et al., 2016).

The carbonaceous base of the Frisco Formation separates it from the chert-rich dolomite of the Eccles Formation which is made up of chert-rich dolomite where this increases towards the top of the Eccles Formation.

The Pretoria Group consists of two geological formations namely; the Rooihoogte and Timeball Hill formations. Rooihoogte Formation, which contains shale and quartzite, consists of alluvial and lake deposit. The Timeball Hill Formation contains shallow to deep marine environment sediments that are made up of shale, diamictite, Klapperkop quartzite, ferruginous quartzites and silty shales (Eriksson et al., 2012).

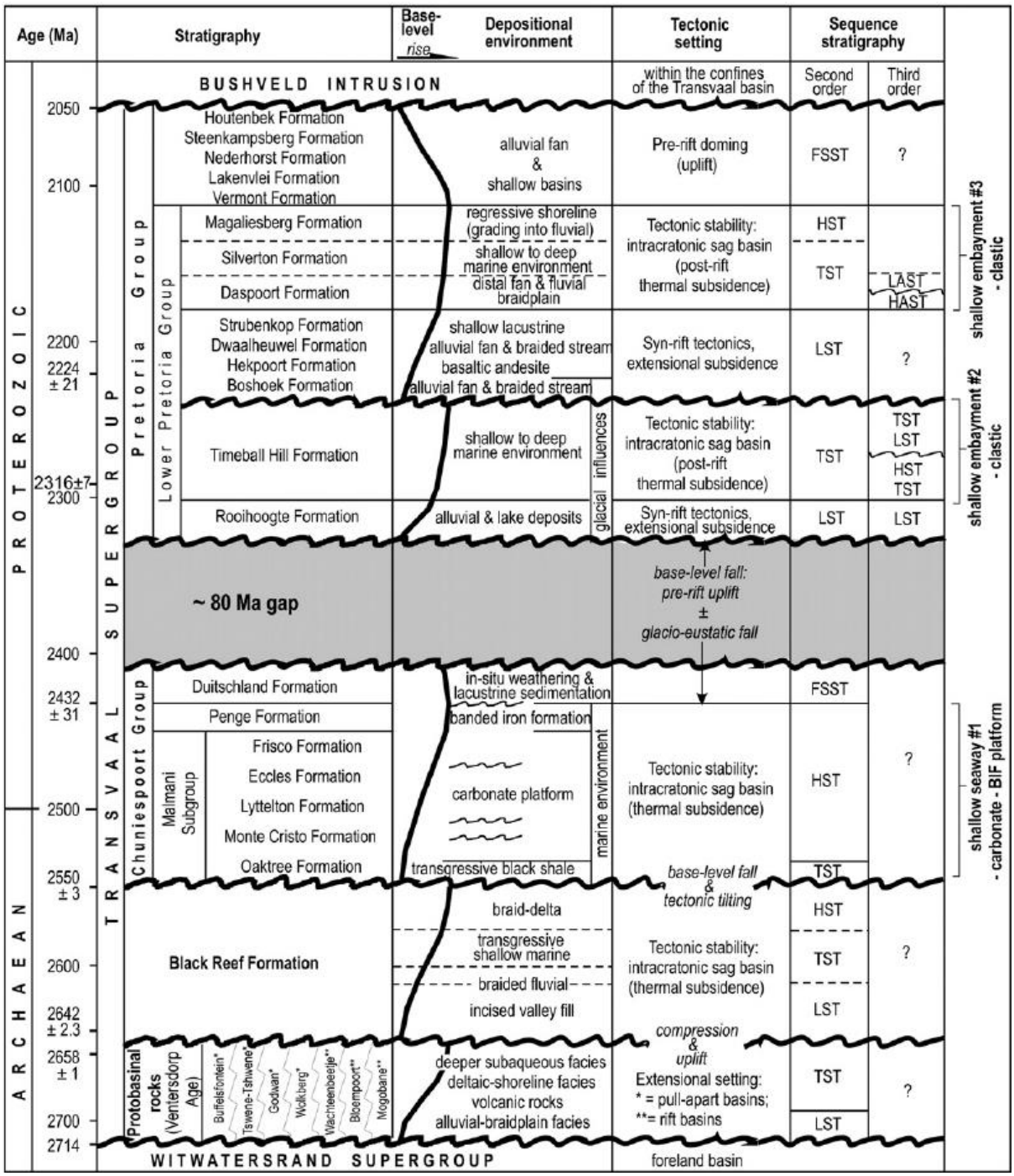

Figure 3: Detailed lithostratigrapy chart which shows the age, depositional environment and sequence stratigraphy the formation of the geological groups that fall under the Transvaal Supergroup. Malmani Subgroup falls under the Chinuespoort Group (Eriksson et al., 2012).

2.3. Water resources of the COH WHS

The COH WHS consist of a number of rivers and tributaries that drain towards the north of the study area. These surface water resources are monitored from four stations. Groundwater resources are also monitored from spring outlets and a number of boreholes that were drilled by the Department of Water and Sanitation.

2.3.1 Hydrology

The springs (A-K) in Figure 4 below measure both the quality and quantity of water that is discharged on a daily basis. The study focuses on 1a, 1b and 1c which discharge into Zwartkrans spring. The quantity focuses on mean, maximum and minimum water discharge while the quality focuses on the full chemical analysis. Such monitoring is done to determine the level of pollution that may be caused by sources such as AMD that discharges into the Tweelopie Spruit and the Percy Stewart waste water treatment works (WWTW) that in turn discharges into the Blougat Spruit as well as the Tweefontein Spruit (Hobbs et al., 2011).

There are several rivers within the system namely: The Bloubank system, Blougat system and Tweelopie Spruit system in Figure 4. The Bloubank tributary flows towards the northeast of the Sterkfontein caves to where it meets the Crocodile River. All the stations plotted on the map in Figure 4 have a 40 year monthly record of discharge measurements. This system, of which the study focuses on, is made up of two drainages namely, the Blougat and Tweelopie Spruits. According to the discharge records, the river had the highest discharges of 66.9 Mℓ/d in 1977/8. Furthermore, the wet summers of 2010 to 2012 also resulted in the second highest discharge in history ranging from 44.9 Mℓ/d to 59.1 Mℓ/d (Hobbs et al., 2011; Hobbs, 2013).

The Blougat Spruit drains towards the northwest of the study area and receives effluent from the Percy Stewart WWTW which is the cause of deteriorated water quality. It was once a seasonal stream, but has now become a permanent stream because of the amount of effluent that it receives from the WWTW. This results in the Blougat Spruit receiving 0.97 Mℓ/d of effluent. The pollution levels have increased due to the plant not being able to treat waste therefore not meeting the effluent quality standards, and therefore resulting in compromised water quality (Hobbs et al., 2011).

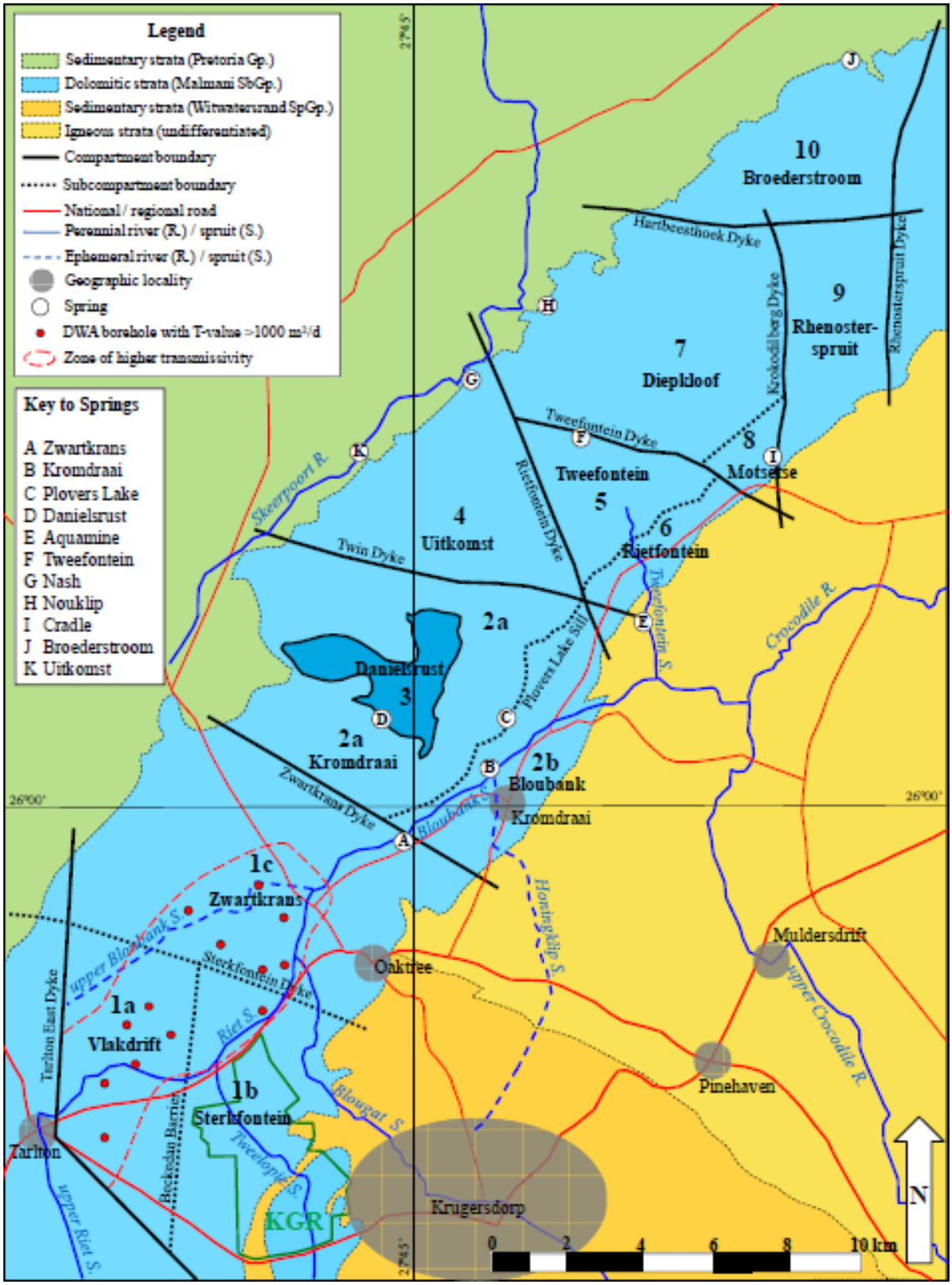

Figure 4: Groundwater flow direction, rivers and spring map showing the compartments and sub compartments of which the groundwater drains towards the Zwartkrans spring. The sub compartments are namely the 1a) Vlakdrift, 1b) Sterkfontein and 1c) Zwartkrans which form part of the aquifer within the study area. The springs are marked as white circles that range from A to K. (Hobbs et al., 2011).

The Tweelopie Spruit on the other hand, receives both treated and raw mine water and once peaked at 50 ML/d after the 2009/10 wet season. Loss of water is experienced downstream which is an indicator of the recharge of the Zwartkrans karst aquifer (Hobbs et al., 2011).

The assessments from the spring outlets have indicated increased levels of SO_4, Na and Cl concentrations. The Percy Stewart WWTW also contributes to the deteriorating water quality of the system with the microbiological impurities such as faecal coliforms. The microbiological concentrations decrease further away from the source of pollution (Hobbs, 2013). Only Cl and SO_4 parameters fall within the South African National Standards (SANS) drinking water quality and the rest exceed it. According to 2010 records, an increase in the amount of some trace metals such as Al and Mn were observed further away from the sources while a decrease in Fe was observed. The major cause for the decrease of Fe is due to the presence of oxygen which enhances precipitation (Hobbs et al., 2011). One of the main contributors to the poor quality of water that does not meet the SANS requirements is the WWTW that discharges industrial wastewater when it was designed to treat only household sewage.

2.3.2 Hydrochemistry

The boreholes within the COH WHS were drilled by the Department of Water and Sanitation to assess and monitor groundwater levels within the study area. A significant groundwater level increase has been observed since 2007 and such aquifer fluctuations have been linked to the summer rains of 2007. The summer rains resulted in the excess discharge to the Tweelopie Spruit. The mixture of mine water and natural discharge resulted in a drainage increase of more than 60 Mℓ/d (Hobbs, 2014). Furthermore, groundwater levels increased towards the north of the study area.

Since there have been mining activities that once took place around the study area, the water quality can be expected to have been compromised. The AMD impact on groundwater can be observed in spring A of the Zwartkrans compartment shown in Figure 4. Sulphates and pH levels were reported to have increased in the central segment with sulphate levels exceeding the required standards. The quality of water improves as one move towards the Zwartkrans spring in the northern segment of the study area (Figure 4). Percy Stewart WWTW and the abandoned gold mine are the main contributors to the deteriorating water quality of the study area. This has resulted in the detection of increasing sulphate levels and decreasing pH levels towards the Zwartkrans spring. However, better groundwater quality is

found at the Zwartkrans spring. The sulphate levels are found to be less than 500 mg/l around the Zwartkrans spring and higher at the south-western parts of the pollution plume (Hobbs, 2013).

2.3.3 Karstic aquifers

The study area is in a dolomite dominated environment that has developed karst conditions through solution of dolomite over the years. Karstic aquifers are formed through a weathering process which results in the dissolution of carbonate rock thereby causing cavities that store water and do not have any form of primary porosity. Furthermore, a chert-rich dolomite has good water bearing properties since chert is brittle. Polluting material tends to have an impact on the aquifer quicker than in the primary aquifers because of high transmissivity that the karst aquifers contain (Holland and Witthuser, 2009).

The COH WHS area is subdivided into 10 compartments which include two compartments that have sub-compartments. These compartments fall in the Dolomitic strata of the Malmani Subgroup and are bordered by vertical dolerite dykes of different permeability that act as water barriers between the compartments, hence the change in water quality between compartments (Hobbs et al., 2011; Holland and Witthuser, 2009). This study focuses only on the Zwartkrans compartment (1a, 1b and 1c) which is located on the southwest of dolomitic strata of the Malmani Subgroup in Figure 4. This compartment is bound by Tarlton East Dyke to the south and Zwartkrans Dyke to the northwest. The Zwartkrans compartment is further subdivided into three sub-compartments that are classified as:

- Zwartkrans Sub-compartment

This sub-compartment covers approximately half of the study area and has the Witwatersrand Supergroup to the southeast and the sedimentary strata of the Pretoria Group to the Northwest. Figure 4 also shows that the Zwartkrans Dyke borders the Zwartkrans sub-compartment to the northeast where it separates it from the Kromdraai compartment. The Zwartkrans Spring located to the northeast of the compartment cannot be accurately gauged since there are other sources that contribute to it such as the Blougat and Bloubank spruits. However, the groundwater discharge is calculated as the combination of the sub-compartments discharge, which is estimated at 24.6 Mℓ/d to 71 Mℓ/d. This sub-compartment also shows mine water pollution trends at lesser concentrations than other sub-

compartments within the Zwartkrans compartment but experiences higher levels of chlorine. The sub-compartment is bordered by the Sterkfontein Dyke to the south.

- Vlakdrift Sub-compartment

Figure 4 shows that the Vlakdrift sub-compartment is located on the southwestern part of the Zwartkrans compartment with the depths to the water table of about 50 m. It shares the Sterkfontein dyke with the Zwartkrans sub-compartment to the north and the Beckendan Barrier with the Sterkfontein Sub-compartment to the west. The south and west of the sub-compartment is bordered by the Tarlton East Dyke. The sub-compartment consists of monitoring boreholes, which indicated that the bacterial impact on water quality is caused by the nearby WWTW. However, the chemical quality of water within the aquifer remains pristine (Hobbs et al., 2011).

- Sterkfontein Sub-compartment

The sub-compartment is located on the southwestern part of the Zwartkrans compartment as shown in Figure 4. It is bound by the Sterkfontein dyke to the North, the Backedan barrier to the west, the Tarlton Dyke to the southwest and the sedimentary strata of the Witwatersrand Supergroup to the west. Mine-water from decommissioned gold mines is the primary source of pollution in this compartment.

The AMD produced from the abandoned mines has a negative impact on the receiving environment and is therefore monitored. The karst environment has higher transmissivity, compared to primary aquifers, which allows mine water to move faster through the aquifer. The elevated sulphate concentration levels can be observed in Figure 5 which indicates the distribution of sulphates concentration within the compartment from south to northeast. The shaded area in Figure 5 indicates the actual pollution footprint by AMD, while the blue arrows indicate the autogenic recharge area which shows the water that is from the karst aquifer, and the orange arrow indicates the allogenic recharge which is the water that is from non karst environment such as the WWTW. This takes into consideration the change in sulphate concentrations further away from the source (Hobbs, 2015).

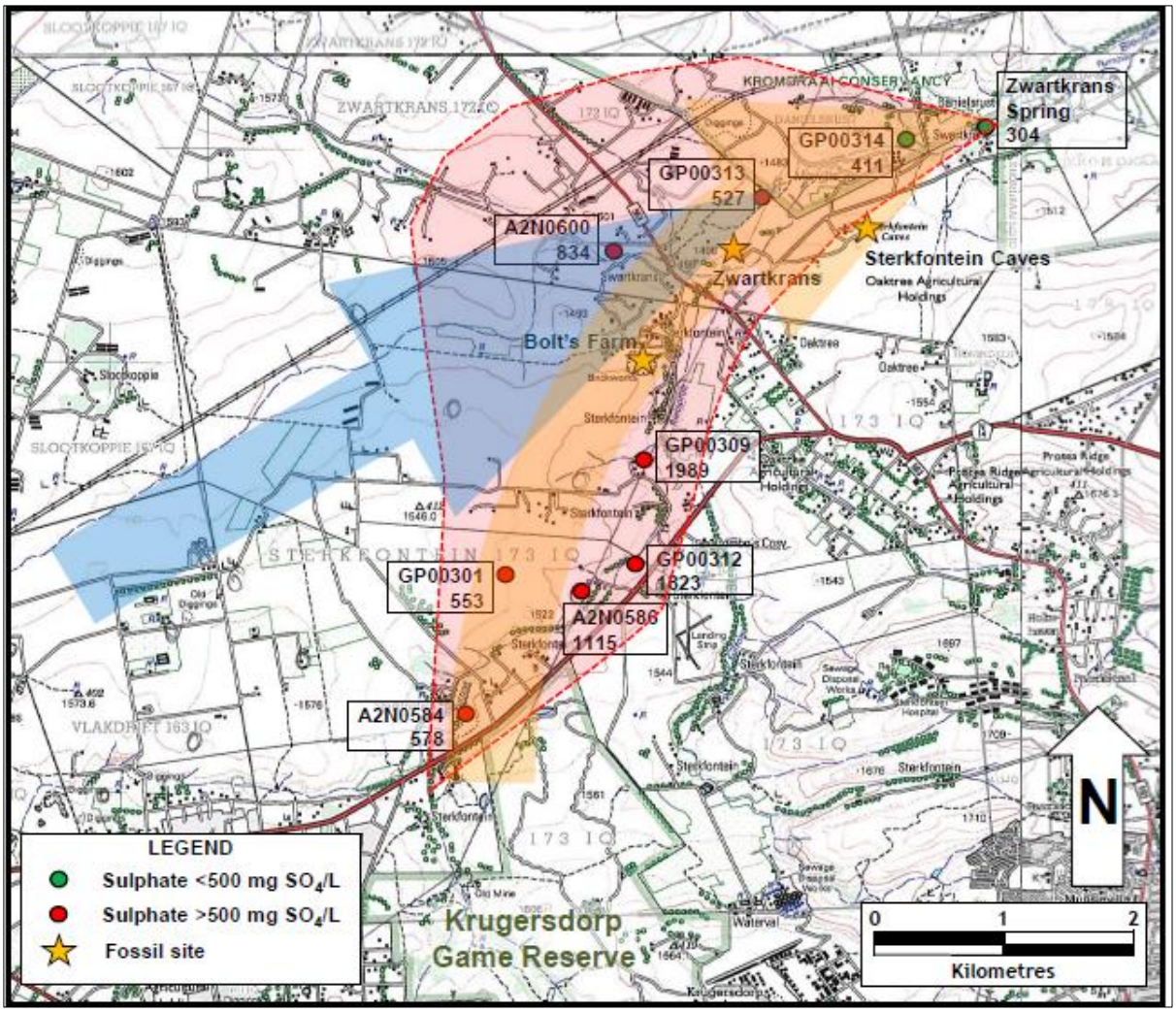

Figure 5: Groundwater movement map showing the distribution of DWS boreholes that measure the sulphate concentration within the Zwartkrans compartment. The impacted area is represented by the light red shaded area while the blue arrow shows the autogenic recharge and the orange arrow shows the allogenic recharge (Hobbs, 2014).

2.4. AMD process

This section describes the chemistry of AMD.

The Pyrite is first oxidized to hydrous ferrous sulphates and their subsequent hydrolysis is the cause of acidity found in most acid mine drainage occurrences. The main chemical reaction is:

$$4\ FeS^{2+} + 15\ O_2 + 14\ H_2O \Rightarrow 4\ Fe(OH)_3 + 8\ H_2SO_4 \qquad (1)$$

Pyrite + Oxygen + Water =>Iron (III) Hydroxide + Sulphuric acid.

Acid mine drainage is a process that follows these steps:

It is the disruption of the Earth during mining that results in the exposure of underlying rock to oxygen, microorganisms, and water which process then result in the oxidation of iron sulphide into dissolved iron, sulphate and hydrogen (Simate and Ndlovu, 2014).

$$2FeS + 7O_2 + 2H_2O \rightarrow 2Fe^{2+} + 4SO_4^{2-} + 4H^+ \quad (2)$$

Pyrite + Oxygen + Water => Ferrous Iron + Sulphate + Acidity

The produced ferrous iron can react with oxygen and hydrogen to produce ferric iron (Equation 3). Such reactions can occur at pH greater than 3.5 but low oxygen concentration hinders the reaction processes to an extent that the reaction may not occur until the pH is greater than 8.5 (Simate and Ndlovu, 2014).

$$4Fe^{2+} + O_2 + 4H^+ => 4Fe_{3+} + 2H_2O \quad (3)$$

Ferrous Iron + Oxygen + Acidity => Ferric Iron + Water

Further reaction which usually occurs is the hydrolysis of iron. The formation of ferric hydroxide precipitate (solid) is pH dependant. Solids form if the pH is above about 3.5. However, below pH 3.5 little or no solids will precipitate. The produced ferric iron further reacts with water where it precipitates (Equation 4) under low pH (2.3 - 3.5) conditions and produces $Fe(OH)^{3-}$ and hydrogen which further reduce the pH (Nordstrom, 2011; Meschke et al., 2015).

$$4Fe^{3+} + 12H_2O => 4Fe(OH)^{3-} + 12H^+ \quad (4)$$

Ferric Iron + Water => Ferric Hydroxide + Acid

Furthermore, the produced precipitate becomes unstable at a pH of lower than 2, and the leftover ferric iron further oxidises pyrite (Equation 5). This reaction will further reduce the pH and result in more acidic water. Further reaction is the oxidation of additional pyrite by ferric iron. This cycle usually continues until ferric iron or pyrite is depleted.

$$FeS_2 + 14Fe^{3+} + 8H_2O => 15Fe^{2+} + 2SO_4^{2-} + 16H^+ \quad (5)$$

Pyrite + Ferric Iron + Water => Ferrous Iron + Sulphate + Acidity

The pyrite oxidation reaction is accelerated and extended by bacteria. The most important of these bacteria are Thiobacillus Ferro oxidants. These bacteria are very active at a very low pH, usually between 4 and 2. The longer that water is in contact with the pyrite, the more chance the oxidation reaction has of proceeding and the more chance bacteria has of speeding it up and producing more acid (Fuggle and Rabie, 1992). The key to the

mobilisation of trace metals in areas where mining has taken place is the oxidation of pyrite, whether the trace metals were locked within the crystal structure of pyrite before oxidation or the trace metals occur due to secondary reactions apart from pyrite. Trace metals already in the environment can also be temporarily mobilised by precipitated hydrous ferric oxides, hydroxides and clay minerals through adsorption under certain pH conditions, and can be precipitated once again by a change in pH.

The Piper diagram in Figure 6 below shows the ideal quality of spring water from the Malmani Dolomite and the impact of AMD on the Sterkfontein Caves and the Zwartkrans Spring water over the years. The diagram shows the breakdown of the amount of cations (bottom left triangle in Figure 6) and anions (bottom right triangle in Figure 6) that the sampled water contains. These further determine the source of water through the use of the middle diamond in Figure 6. In the case of the study area, the deteriorating water quality changes can be observed between two timeframes before and after 2014. An increase in sulphate concentration can be observed in the Sterkfontein caves as well as at the Zwartkrans Spring compared with the ideal karst springs represented by the blue dot in Figure 6 (Hobbs, 2014).

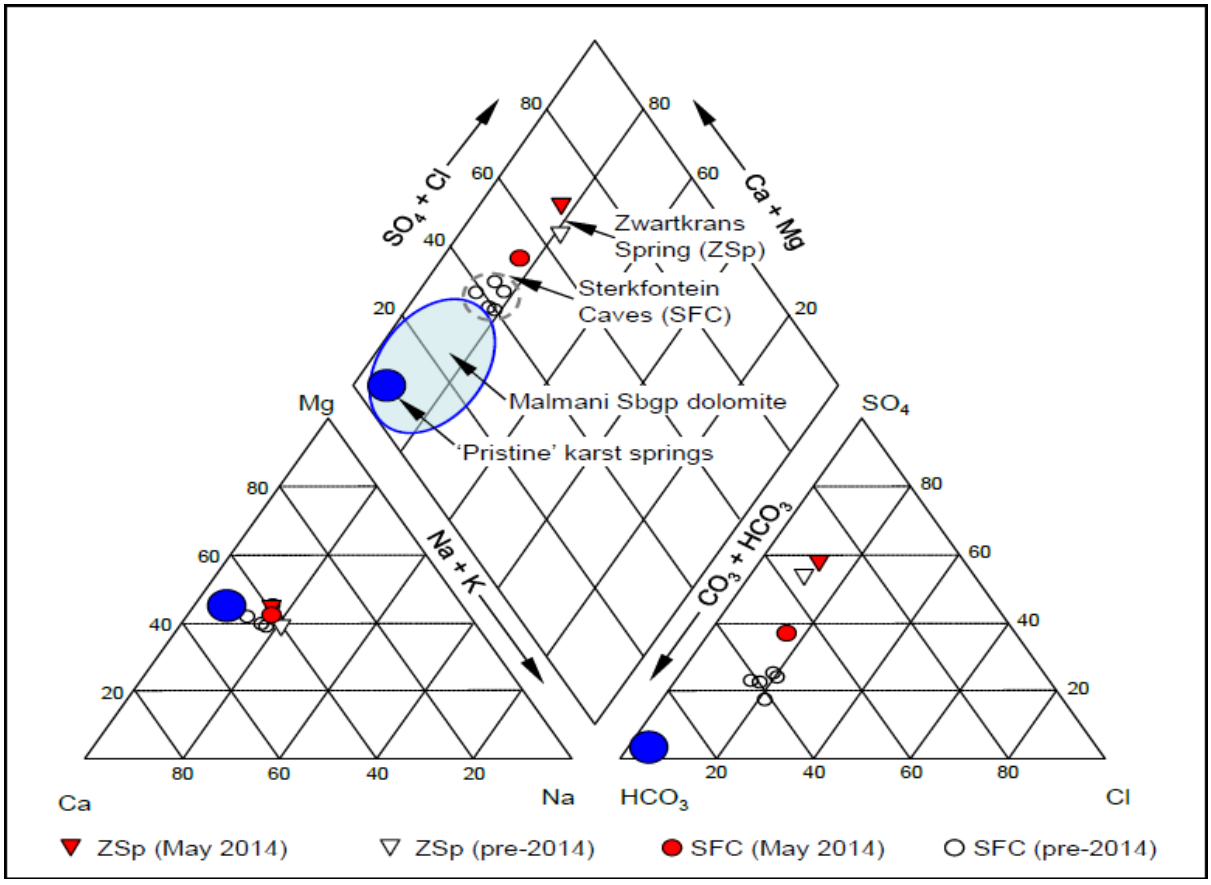

Figure 6: Piper diagram showing the ideal groundwater quality from karst springs and the spring water quality from the dolomite of the Malmani Subgroup (circled in blue). Groundwater quality from Sterkfontein Caves (circle) and Zwartkrans spring (inverted triangle) is shown in white for pre-2014 and red for post-2014 (Hobbs, 2014).

2.5. Other study area factors

Rainfall

According to 2008 to 2015 precipitation records from the areas surrounding the study area, the rain gauge located next to the pollution source (high density sludge) recorded a highest reading of 575 mm of rain during the wet season of 2008 to 2009. The Sterkfontein cave measuring station recorded a highest of 542 mm/year in the 2011-12 wet season since the assessments started. The recharge levels did not have much impact on the already polluted groundwater which still fell within the treatment capacity of the 34 Mℓ/d treatment plant. However, the mean annual precipitation measurements from nearby stations indicated a total of 734 mm and 809 mm, respectively between the wet seasons of 2009/10. Higher rainfall levels have a potential to flood the groundwater systems which may result in treatment process capacity being exceeded. The infiltration levels are higher during wet seasons from November to January and lowest in winter (Hobbs, 2015).

3. ELECTRICAL RESISTIVITY BACKGROUND

Geophysical surveys are conducted to obtain subsurface geological information, generally without having to drill into the Earth and these surveys are often non-invasive. A wide variety of geophysical methods exist to serve different purposes that range from delineation of pollution plumes, geological structures to mineral and groundwater exploration (Chandra et al., 2011; Loke et al., 2013; Orlando, 2013). Geophysical surveys can either be passive (natural source methods) or active (controlled source methods). Methods that gauge naturally occurring phenomena such as the Earth's magnetic and gravity fields are regarded as passive methods. The active geophysical methods, on the other hand, focus on introducing external source fields into the Earth in order to assess the resulting response. The response is guided by the underlying factors such as the geology, water saturation content by minerals, water content within the rocks and permeability of the rocks (Descloitres et al., 2008; Wagner et al., 2013).

In the CSIR/WRC project, on which this study is based, the geophysical method of choice was the ERT method. Since the project is focusing on the monitoring of groundwater contamination progression, the time-lapse ERT method has the ability to represent the electrical resistance variations in the aquifers, which may be related to changes in the level of AMD pollution (Clément et al., 2009; Orlando, 2013;).

The main (WRC) project focused on the use of ERT method, using the multi-gradient electrodes array to obtain field data. The data were inverted to produce 2D tomograms which represented snapshot images of the plume and further assessments will determine the plume advancement (Descloitres et al., 2008; Chandra et al., 2011). As part of the WRC study recommendations, this study focuses on the numerical modelling of time-lapse ERT using synthetic data to determine the minimum resistance contrast between the target and host rock that can be detected by the ERT method. For this project, the actual field data were used for modelling.

This chapter discusses the basic concept of the direct current electrical resistance method as well as the multi-channel approach of ERT method that involves the acquisition large data sets and also tomographic imaging. Latest developments in computational systems have resulted in the advanced modern day data processing techniques of ERT data, which is a significant advancement from the conventional graph-based interpretation methods (Binley and Kemna, 2005).

3.1 Basics of electrical resistivity

Direct current measurement is one of the most used geophysical tools to assess the shallow subsurface electrical response to induced currents in the least invasive manner (Binley and Kemna, 2005; Kuras et al., 2009; Loke et al., 2013; Mao et al., 2015; Power et al., 2015). However, there is no limit to the depth that the method can assess and such assessments have been conducted to assess the Earth's upper mantle (Van Zijl, 1977). Electrical resistivity is governed by Ohm's law which states that the electric current is inversely proportional to resistance and directly proportional to voltage as shown in Equation 6. The applicability of Ohm's law to calculate the potential difference on a continuous medium uses finite element method (FEM) to solve Poisson's equation (Loke et al., 2013; Liu et al., 2014). This equation allows the calculation of the potential differences due to an injected current and the measured apparent resistance (Van Zijl, 1977). This tool characterises the subsurface formations through their response to induced current. Electrical resistivity is controlled by factors such as the concentration of dissolved ions in water, ore minerals in the Earth and fractures in rocks (Binley and Kemna, 2005; Mao et al., 2015). A wide range of resistivity values for Earth materials is possible, as shown in Figure 7.

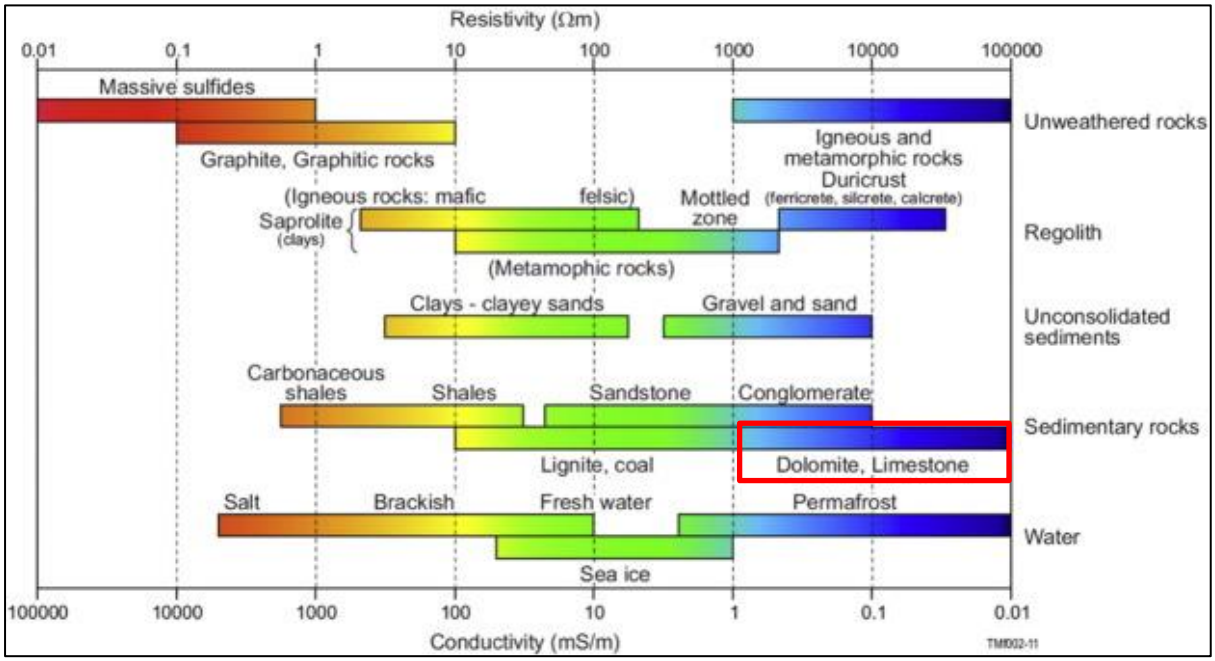

Figure 7: Conductivity and resistivity values for different geological material. The resistivity of the study area (dolomite) is marked by a red square which shows that it is a sedimentary rock that falls within the resistivity magnitude of 1000 to over 10 000 Ωm (González-Álvarez et al., 2016).

Direct current resistance measurements are conducted by injecting current (I) into the ground using two current electrodes and using potential electrodes to measure the voltage difference as shown in Figure 8 below. These current and voltage measurements can then be converted into apparent resistivity (Giguère et al., 2008; Loke et al., 2013). The current travel density (J) in a homogenous subsurface with equipotential layers and the electric field (E) can be described by the vector form of Ohms law as shown in Equation 6.

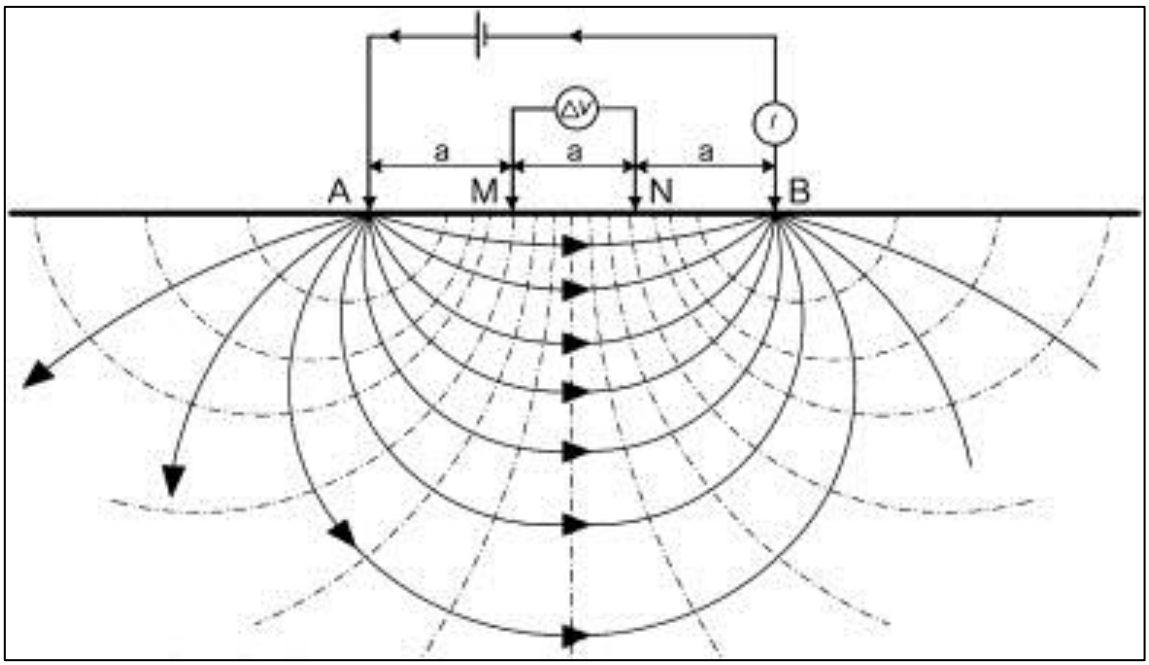

Figure 8: A depiction of a Wenner array whereby current electrodes (A, B) and potential electrodes (M,N) on a homogenous half space. The equipotential lines indicate the scenario of a homogenous Earth and (a) is the distance between electrodes (Wiwattanachang and Giao, 2011).

$$J = \sigma E = \frac{1}{\rho} E = -\frac{1}{\rho} \nabla V \quad (6)$$

Equation 7 is practical if the conditions that mimic Figure 8 where equipotential surfaces are perpendicular to the current direction from one electrode. These equations can be further developed to consider the geometry of actual resistivity measurements involving a pair of current electrodes and a pair of voltage electrodes.

$$\frac{V}{I} = \frac{\rho L}{A} \quad (7)$$

The voltage values at the respective potential electrodes (M and N) are given by Equations 8 and 9 and the total potential difference is given by Equation 10:

$$Vm = \frac{\rho I}{2\pi}\left(\frac{1}{AM} - \frac{1}{MB}\right) \quad (8)$$

$$Vn = \frac{\rho I}{2\pi}\left(\frac{1}{AN} - \frac{1}{NB}\right) \quad (9)$$

$$Vmn = Vm - Vn = \frac{\rho I}{2\pi}\left[\left(\frac{1}{AM} - \frac{1}{Mb}\right) - \left(\frac{1}{AN} - \frac{A}{NB}\right)\right] \quad (10)$$

Therefore the apparent resistivity can be derived from rearranging the potential difference equation 10 and the geometric factor of K (Equation 11):

$$K = 2\pi\left[\left(\frac{1}{AM} - \frac{1}{MB}\right) - \left(\frac{1}{AN} - \frac{1}{NB}\right)\right] \quad (11)$$

Therefore the resistivity is given by

$$\rho = \frac{Vmn}{I}K \quad (12)$$

The factors M, N refer to the potential electrodes and A, B refer to the current electrodes in Figure 8. The potential difference depends on the location of the electrodes, and the further current electrodes are from the potential electrodes, the weaker the amount of the voltage that will be recorded. The opposite is true (Ewusi, 2006).

Traditionally, electrical resistivity field data are collected using either a sounding or profiling approach. The vertical electrical sounding (VES) method focuses on assessing vertical resistivity variations, while the electrical resistivity profiling method focuses on assessing the lateral variations at the same depth over a distance that is being assessed. The modern ERT survey approach essentially combines the sounding and profiling principles to get lateral and vertical information from the same data.

3.2 Electrode configurations used in electrical resistance surveys

Both survey designs were once regarded as time consuming. For soundings, the distance between the current electrodes is varied while potential electrodes remain stationary in order to obtain more depth variation information. On the other hand, the profiling focuses on obtaining lateral variations within the study area. The design has a fixed distance between the electrodes, with the whole electrode (potential and current) array being moved across the same line to assess the resistance at the same depth level. The profiling depth depends on the electrode spacing; wider spacing is used to assess lateral variations at greater depths and the opposite is true for shallower investigations.

The closer the potential electrodes are to current electrodes, the better the signal-to-noise ratio. In addition, the background noise must not overshadow the field anomalies in order to ensure meaningful interpretation of the data. Interfering electrical noise is generated by nearby electric conductors such as fences and buried steel pipes. The optimum choice of electrode configuration is based on factors such as signal-to-noise ratio, depth to the target, water content, porosity, lateral coverage and the size of the target (Brunet et al., 2010; Chandra et al., 2011; Mao et al., 2015; Power et al., 2015; Zeng et al., 2016).

The mapping resolution depends on the configuration of electrodes whereby more width between current and potential electrodes has less lateral sensitivity and higher vertical sensitivity in the case of VES (Jones et al., 2012). The signal-to-noise ratio is also determined by the closeness of potential to current electrodes, which is high if electrodes are closer and low if they are far from the current electrodes (Dahlin and Zhou, 2006). The most common arrays for VES and profiling are shown in Figure 9. Such methods focus on assessing the resistivity variations with depth which depends on factors such as aquifer thickness, depth to the aquifer, aquifer contamination and stratigraphy of the area. The gradient array is one of the arrays that can be solely used for profiling, while other arrays can be used interchangeably. A brief description of the various arrays is as follows:

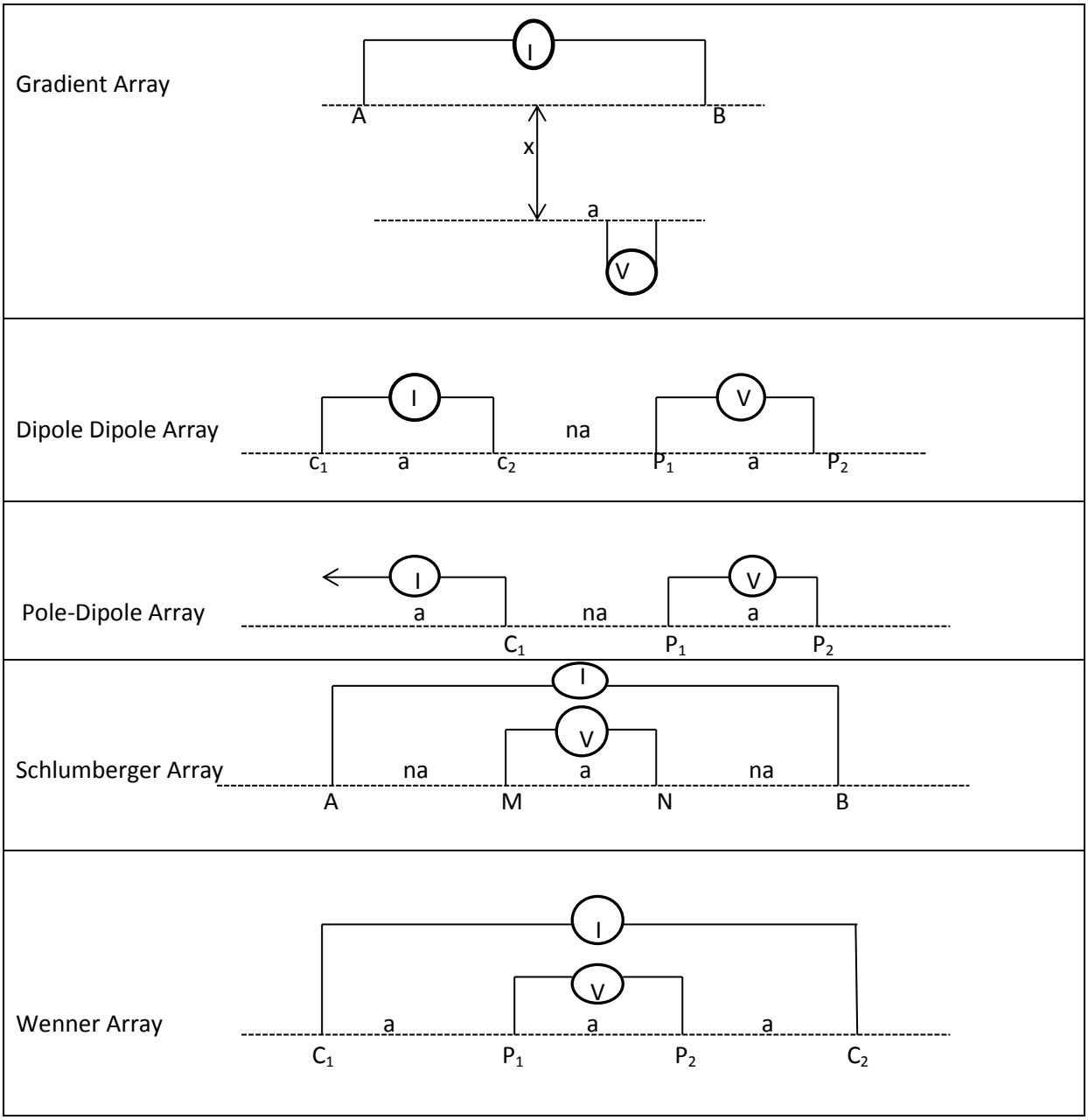

Figure 9: The displayed configurations can conduct a sounding or profiling assessment, but it is the purpose for the study that determines their feasibility most preferable uses (modified from Ibeneme et al., 2013).

Gradient array

Multi-gradient array is a nonconventional array in which the current electrodes are kept at a minimal distance apart to assess the maximum potential measurements per survey. This array is well suited to the assessment of lateral variation within the subsurface. It has been previously indicated that the choice of array depends on both the survey requirements and the level of sensitivity required in obtaining quality data. The multi-gradient array's ability to

simultaneously record many data points for a single current injection without compromising the data quality gives it the advantage over the conventionally used arrays such as Dipole Dipole, Schlumberger and Pole Dipole (Dahlin and Zhou, 2006).

Dipole Dipole array

This array uses a 2 pairs of electrodes whereby the current electrodes are equally spaced and the potential electrodes are moved further and further away from the fixed pair of current electrodes. This array has the ability to sample a large number of data points and is suitable for the VES of sub vertical formations such as dykes at shallow depths (Dahlin and Zhou, 2006; Jones et al., 2012; Zeng et al., 2016). Furthermore, this array is easy to conduct in the field because of the least amount of short wires but more power is required as one conducts deeper VES.

Pole Dipole array

The asymmetrical configuration of Pole Dipole array which has 2 current electrodes of which one of them is located at a distance and potential electrodes is shown in Figure 9. The small distance between the current and potential electrodes makes the Pole Dipole array less prone to noise than the Pole Dipole array that has a much wider distance between the electrodes. Asymmetrical results that are acquired using the Pole Dipole array are not as easy to interpret as the other data acquired using symmetrical arrays hence the need to repeat the surveys by reversing the orientation of the array.

Schlumberger array

This array, shown in Figure 9, places the current electrodes on the outer ends of the array and places the potential electrodes on the inside where the electrical sensitivity will be the highest. The array moves only current electrodes while the potential electrodes remain at a fixed position in order to increase its VES. This allows deeper assessments as the current electrodes are moved further away from potential electrodes. This array has been successfully used in sounding assessments as well as profiling (Van Zijl., 1977; Buselli and Lu, 2001)

Wenner array

The Wenner array has one of the greatest signal strength but has a high close to surface noise level detection and requires minimal data to construct a pseudo section. This method is ideal for VES. It has been proven to be less likely to be affected by noise when compared against more sensitive arrays such as the Dipole Dipole and Schlumberger array (Clément et al., 2009; Wagner et al., 2013).

Wenner-Schlumberger array

This hybrid array is used for simultaneous sounding and profiling surveys. Its signal strength is stronger than that of dipole-dipole array, but weaker than the Wenner array. This combination shares both characteristics of the arrays but does not perform as well as any of the individual techniques on which it is based. The Wenner-Schlumberger array is most applicable in the assessments of changes in resistance both vertically and horizontally, but the data quality weakens as the survey depth increases (Wagner et al., 2013; Power et al., 2015).

The abovementioned arrays are used to collect field data and the multi-gradient array was selected for this study because it met the study requirements which were to assess the lateral variation within the aquifer. The variations are driven by the change in the amount of dissolved minerals that are present in the water. The multiple-gradient approach has the ability to produce similar if not better resolution images than the Wenner and Dipole Dipole arrays that are most commonly used in 2D imaging processes and has proven to be better than other models because it is economical and less time consuming (Dahlin and Zhou, 2006; Loke et al., 2013).

3.3 Electrical resistivity tomography

Electrical resistance imaging or tomography (ERT) is the new popular method of data representation that evolved from the previous 1D graph presentation shown in Figure 10. With traditional electrical soundings, for example, the results from the field survey had to be fitted against a master curve when using the 1D model. A new approach which uses multicore cables and multi-channel resistivity meters drastically reduces the amount of time

that is spent on the data collection and can simultaneously assess depth and lateral variations from one survey (Mao et al., 2015).

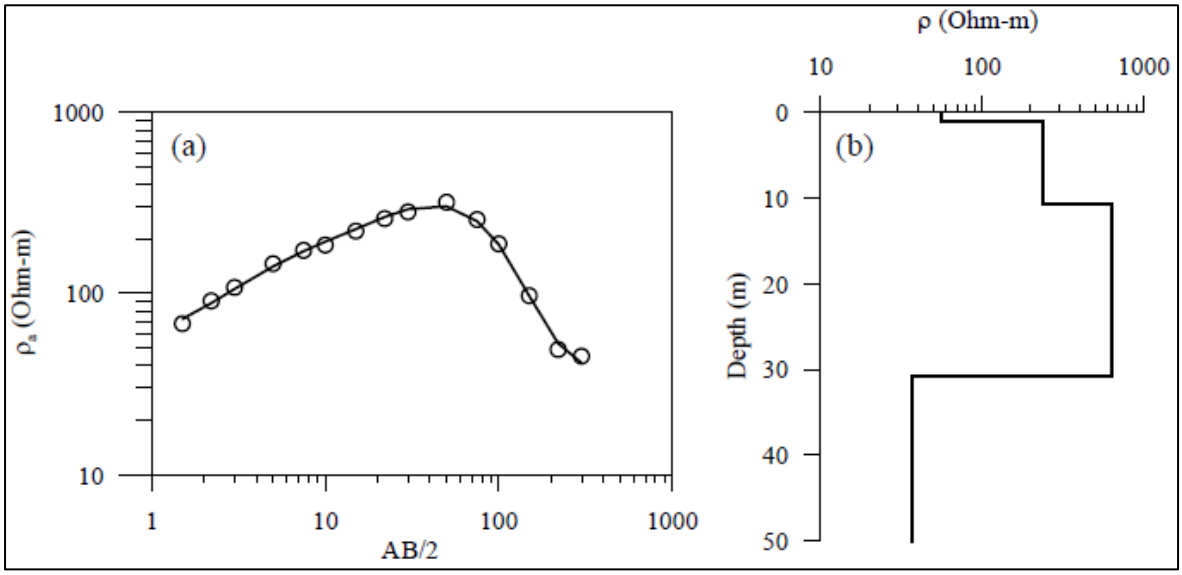

Figure 10: Typical sounding technique representation by the Schlumberger array over a single point showing the geoelectric variations. Note that the circles represent the data points. The right image represents the model curve for the single assessed point (Binley and Kemna, 2005).

Further advancement in the computer technology has led to better and faster data processing algorithms which are widely used to improve the subsurface mapping resolution. These software and hardware improvements enable the collection and processing of much bigger data sets using any of a variety of measurement schemes (see for example Figure 11).

ERT is a process of converting data that are obtained from the field using different arrays (Figure 9) into a representation of subsurface resistance and computer software such as Res2DInv, ZondRres2d and other models have been used to process data by means of inversion (Descloitres et al., 2008; Giguère et al., 2008; Orlando, 2013; Power et al., 2014).

Further experimental forward and inverse modelling (or computer simulations) has allowed the representation of field conditions to obtain potential results that can be used to plan or improve field surveys.

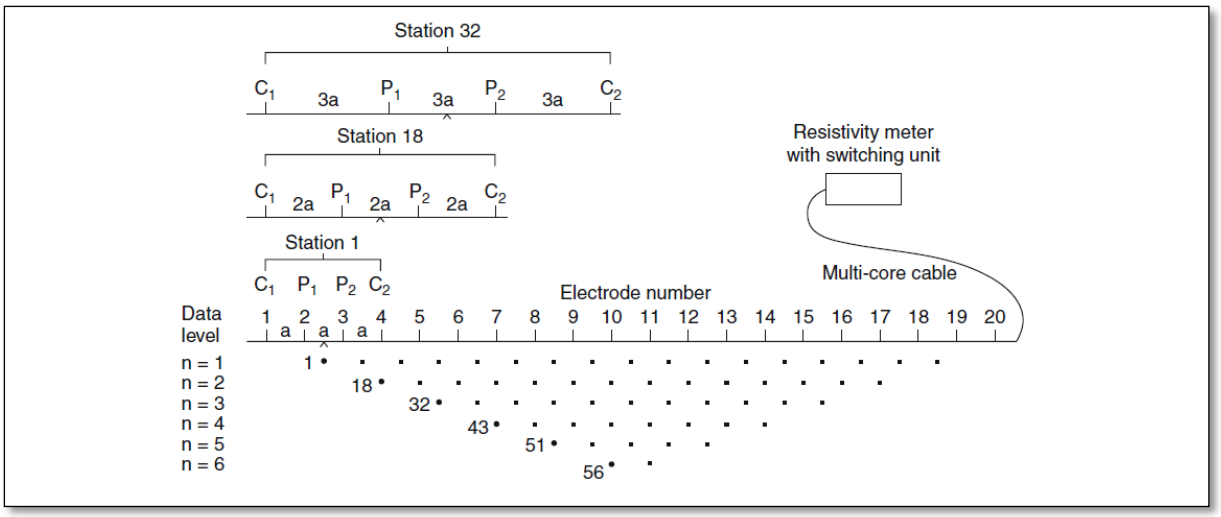

Figure 11: Electrode arrangement for a 2D Electrical survey to construct a pseudosection for forward modelling through the repetition of measurements. A pseudosection is a collection of data levels obtained from individual stations during the survey. Lower data levels (closer to the surface) are obtained by closer spaced electrodes while deeper levels are obtained as the electrode space increase (Shaaban and Shaaban, 2001).

The ERT allows one to visualise lateral and depth variations of the assessed area as shown in Figure 12. The image also shows the different subsurface resistance levels. The WRC project mentioned earlier focused on using the 2D imaging in order to map the subsurface properties of the aquifer.

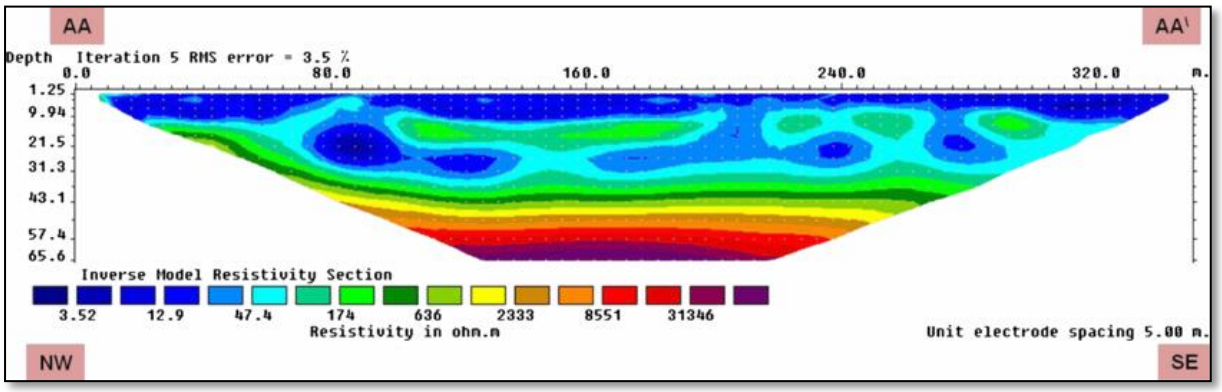

Figure 12: A Res2dInv tomographic output using Wenner array depicting geoelectric resistivity variations of the assessed area, resistivity variations according to the scale at the bottom left can be seen on the tomogram. The traverse direction is shown on the bottom corners (Loke et al., 2003).

3.3.1 The forward model theory

The forward model can be regarded as a pre-requisite for the inverse model because it determines the apparent resistivity that is required in inverse modelling to be compared against real resistivity values. The forward problem can be solved using techniques such as integral equation method, finite difference or FEM. An actual survey can then be simulated by specifying the same electrode array that would be used in the field. Geoelectric models are usually simplified as a homogeneous background with some anomalous localised resistance structures of different resistance. Furthermore, the study area can be represented by a grid of cells that have different resistivity values as shown in Figure 13 (Nguyen et al., 2005).

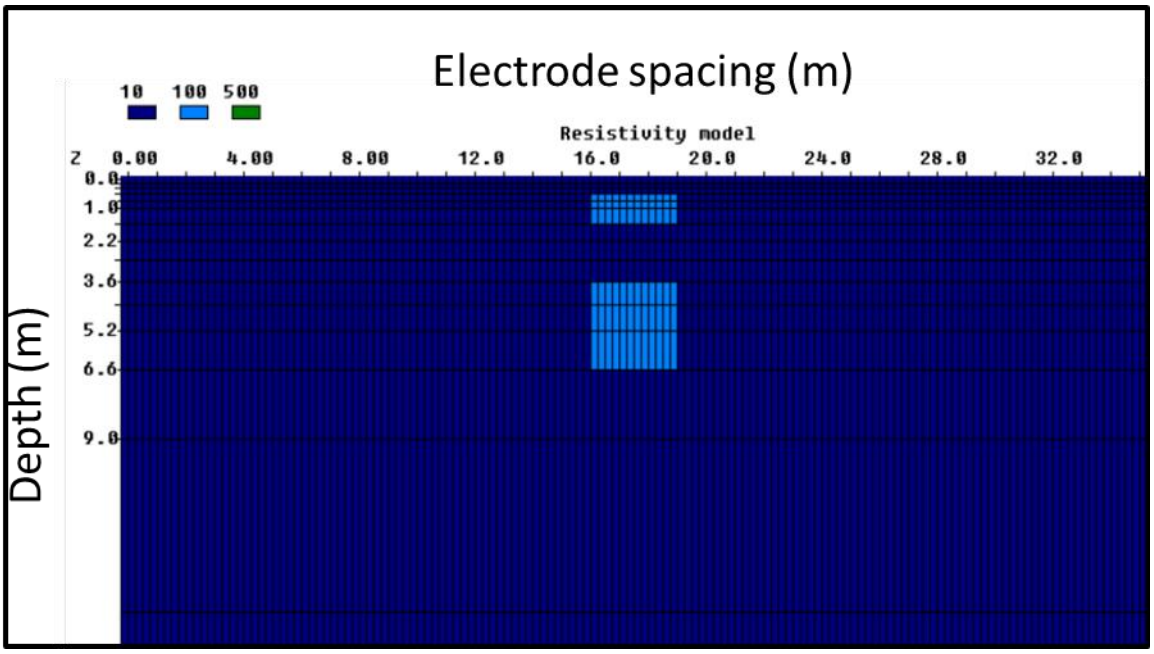

Figure 13: The grid is the initial step in geoelectric modelling where the light blue squares represent synthetic data variations that will be modelled using Res2DMod. The increase in resistivity is modelled by the use of the scale on the top left. The electrode spacing and the traverse length are displayed on the horizontal scale while the vertical scale represents the depth.

The synthetic data are utilised in the same way as the authentic data and made realistic by introducing Gaussian noise (Orlando, 2013; Wagner et al., 2013). The use of a three stage modelling approach focuses on the use of; a) synthetic model where superficial data are used for mimicking real life conditions, b) inversion of superficial data to produce ideal field conditions, and c) advanced time-lapse inversion which uses existing information to create ideal conditions that can be incorporated into the model in order to produce better quality results (Clément et al., 2009).

A snapshot of synthetic data assessment begins with the use of a layer with homogenous resistance that is set as a baseline and then proceeds to adjust the parameters until the ideal apparent resistance threshold is reached (Orlando, 2013; Rucker, 2014). As for the ideal threshold value, different threshold numbers are used to model real world conditions. This modelling process employs the input of different resistivity values of the investigated target, ideal electrode spacing and noise free synthetic data which are generated through the use of FEM (Tsourlos et al., 2014). The results obtained from the model are always compared against the field results in order to validate the models (Wagner et al., 2013).

Furthermore, repetition of simulations is advantageous because it bridges the error estimation gap thereby reducing the artefacts and unrealistic smoothing of data. Over-smoothing is also avoided by reducing the difference between the measured and the calculated apparent resistance (Wagner et al., 2013; Power et al., 2015; Giampaolo et al., 2016).

3.3.2 Inversion theory

The inversion process seeks to estimate a model response and parameters that represent the field measured data through mathematical representation. This is done through the reduction of differences between the ideal Earth (homogenous half space) model and the actual field collected data. The reduction of the differences is a process called optimisation which reduces data impurities until the difference between the field data and the model data is minimized. However, data must be limited because inversion algorithms are not efficient in processing large amounts of measured data (Tsourlos et al., 2014; Power et al., 2015).

The use of algorithms must be efficient enough to efficiently perform inversion of required ER lines without compromising the space of the Jacobean matrix by excluding minor distance entries from the sensitivity matrix. This therefore allows the use of Least-Squares regression when conducting inversion which does not require a lot of memory and time to execute (Tsourlos et al., 2014).

The model response and parameters are mathematically linked using FEM and finite difference methods to represent the field subsurface conditions. This process converts the subsurface into blocks in order to display the density of the assessed data. In addition, the Least-Squares equations are solved using the Gauss-Newton equation (Descloitres et al., 2008; Chandra et al., 2011; Aizebeokhai and Oyeyemi, 2014; Giampaolo et al., 2016). The

model must have the closest response to the collected field data, and this is done through an optimisation process that uses a variety of equations to reduce the gap between the field data and the modelled responses (Loke et al., 2013). The model response and field data are written as a column vector of which the logarithm for the apparent resistivity values from observed and model responses addresses resistance problems. The model columns remain similar between model and field data representation.

The error squares reduction in the modelled and observed data is addressed by the further modification of the discrepancy vector G. This is done through the use of Gauss Newton equation on model parameters. However, the use of Gauss Newton equation produces large components that produce unrealistic results which do not provide the solution for the change in apparent resistivity values. This results in the use of the damping factors through the Least-Square optimization method (for 2D model) that limits the numerical artefacts that the vector can use (Loke et al., 2013).

The smoothing process removes noise from the dataset using algorithms. The smoothing process is executed by modifying the Gauss-Newton Least-Square equation to reduce the spatial variations in model parameters to accommodate the gradual change of resistance values (Loke et al., 2013). Further modifications to the Least-Square equation give better resistance values through the blocky inversion method. This allows the equal weighing of vectors such as data misfit and model roughness in the inversion process.

4. METHODOLOGY

4.1. Background

ERT modelling typically involves forward modelling (the mathematical processes to calculate the resistance response of a known/estimated geoelectric model) and inversion (essentially, the reversal of the same process in which the model is estimated which is responsible for the observed apparent resistance). Inversion is an iterative process in which the apparent resistivity of an estimated model is adjusted until its response fits the observed resistivity (Binley and Kemna, 2005; Power et al., 2015; Giampaolo et al., 2016). Different algorithms have been developed to solve resistivity forward and inverse models. This study focuses on the use of CRMod and CRTomo (Kemna, 2000) that differs from other well-known software such as RES2DINV (Loke and Barker, 1996) in that it uses a complex resistivity (CR) formulation.

As stated earlier, the focus of this study is on the numerical modelling (computer modelling) of the time-lapse ERT approach as it pertains to the WRC project on which this study piggy-backs. The WRC project involves a sense of baseline ERT surveys at selected sites, which were conducted in late 2015 and early 2016. The intent of the WRC investigation is to repeat the surveys in mid-2017 and use the data to perform a time-lapse analysis (essentially using a different tomography approach) to possibly detect subtle changes in aquifer resistance over the 12-18 months period between the baseline and repeated surveys. Such changes in resistance could then possibly be attributed to changes in the pollution levels of the aquifer.

The model study therefore takes place between the completed baseline surveys and the pending repeat surveys and is aimed at predicting the performance and limitations of the proposed time-lapse approach although the baseline survey will not feature as a pertinent part of this study. The results from those surveys were used as input parameters to better design the basic geometric models in this study.

In this chapter, the modelling that is used in this study is discussed in detail.

4.2. Forward modelling using the CRMod

The forward modelling approach used in CRMod focuses on the modelling of complex electrical potentials through the extension of FEM. In a complex formulation, geoelectric models are defined as a complex resistivity distribution. In other words, resistivity elements

are assigned a resistivity magnitude and a phase value. This enables the modelling of both resistivity and induced polarisation (IP) responses. The focus will however be on resistivity (magnitude) response.

The FEM method is used to solve Poisson's equation shown in Equation 13, where j_s is the current density and σ is the electric conductivity.

$$\nabla\cdot(\sigma(\omega)\nabla\phi)) - \nabla\cdot j_s(\omega) = 0 \quad (13)$$

Poisson's equation is solved for point current sources and transferred to the wavenumber domain. This results in a two-dimensional Helmholtz equation that is numerically solved.

The geoelectric model uses FEM to discretize the elements into homogenous finite elements in which its conductivity is assumed to be constant (Kemna, 2000; Van Schoor, 2009; Oberdörster, 2010).

$$\partial_x\left(\sigma\partial_x\widetilde{\phi}\right) + \partial_z(\sigma_\partial\phi) - \sigma k^2\widetilde{\phi} + I\delta(x - x_s)\delta(z - z_s) = 0 \quad (14)$$

Further modification of Helmholtz equation allows the modelling of the boundary conditions for surface (air) and half space (subsurface medium). In order to reduce errors during modelling, a larger amount of grid elements is required and such large grids cover more than the required assessment space which results in higher computing power requirements. This challenge is mitigated by the use of mixed boundary conditions which can drastically reduce the amount of quadrilateral spaces therefore reducing the computing time required for the model (Kemna, 2000).

The numerical solution ultimately reduces to the evaluation of a complex system of linear equations of the term:

$$b = S\widetilde{\phi_s} \quad (15)$$

Where S is the FE matrix and $1\widetilde{\phi_s}$ is the transformed potential vector.

4.3. Inversion using CRTomo

The inversion process seeks to find a model that represents a field or a true geoelectric model. The inverse problem requires a solution of the model vector (m) and the data vector (d). The model vector (m) has the properties of the soil conductivity while the data vector (d)

has the voltage properties which are log transformed resistances. The property M in the model vector (m_j) is the number of parameters and σ_j is the logarithm of bulk soil resistivity (Equation 16), while the property N in the data vector (d_i) is the number of measurements, and R_i is the log transformed resistance as shown in equation 17 (Kemna, 2000; Oberdörster, 2010).

$$m_j = In\sigma_{b,j} \quad (j=1,\ldots, M) \tag{16}$$

$$d_i = LnR_i \quad (i=1,\ldots, N) \tag{17}$$

The complex resistance inversion model uses the Tikhonov regularisation approach which is the most common approach when solving complex resistance problems. This approach is used to solve for underdetermined and ill-posed inverse problems in Equation 18 (Van Schoor, 2009). The non-uniqueness of the problems yields infinite possible models which are then regularized in order to derive the one unique model that has the qualities of the assessed area. The Tikhonov approach is minimized through the following equation:

$$\Psi(\mathrm{m}) = \Psi_d\,(\mathrm{m}) + \lambda\Psi_m\,(\mathrm{m}) \tag{18}$$

The cost function that is minimised is represented by $\psi_m^{(m)}$, and λ is a regularization parameter that ensures that the model adheres to predetermined parameters. The model functions containing the required characteristics are represented by $\psi_m^{(m)}$,

$$\Psi d(m) = \sum_{i=1}^{N} \frac{|d_i - f_i(m)|^2}{|\varepsilon_i|^2} \tag{19}$$

The data misfit is measured by Chi-squared where each data point is contaminated by the Gaussian noise and data error (d_i). The forward operator is then denoted by f_i in Equation 18 and the Root Mean Square is the error and is given by Equation 20.

$$\epsilon^{RMS}(m) = \sqrt{\frac{\Psi_d(m)}{N}} \tag{20}$$

A standard Gauss-Newton method is applied together with a conjugate gradient (CG) method to solve the numerical problem. The minimisation of the global objective is subject to the iterative process until a satisfactory data misfit value is reached, and a trial and error approach is used to determine the optimum regularization value.

4.4. Image appraisal

In the ERT, the concept of image appraisal is often mentioned. This refers to a determination of the spatial variation in image resolution (Figure 14). In other words, this determines how the chosen survey geometry, inversion parameterisation and measurement errors affect the resolution in different parts of the survey area. This can be done by calculating a normalised accumulated sensitivity map through the use of CRTomo software which has a built-in option to calculate such maps (Van Schoor, 2009).

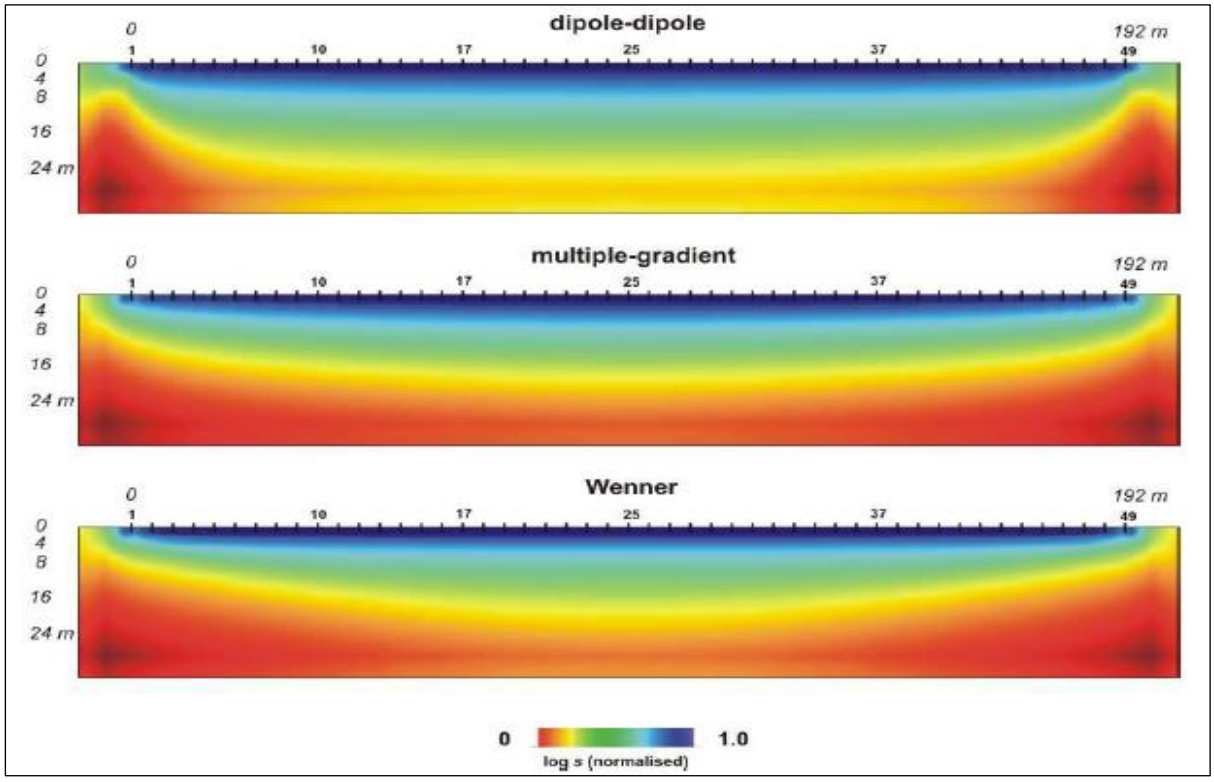

Figure 14: The inversion outputs depict the sensitivities when using different arrays. The arrays look similar to an untrained eye. However, the Dipole Dipole array has low signal strength the edges but more sensitive in the middle, hence the thick green space and also at depth, this makes it more ideal for both sounding and profiling. Wenner array is least sensitive at the edges and bottom which makes it more ideal for profiling than sounding. The multi-gradient is has the best of both arrays which makes more ideal for profiling.

4.5. Computer simulations

The aims, questions and objectives of the model study were highlighted in Chapter 1 and the methodology used will be explicitly described below.

A range of simplified but realistic geoelectric models that potentially represent karst aquifer scenarios will be defined. The process starts with the development of the mesh (grid) that is

used throughout the study. The electrode configuration and measurement sequence is determined. The forward model is calculated to generate the synthetic data. A small level (<2%) of Gaussian noise is then added to the data prior to inversion to mimic field conditions and prepare it for the inversion process in order to generate the final output image.

The main variable in the model is the relative change in the target properties. The resistivity change is adjusted to represent a different contrast between the baseline model's target resistivity and the subsequent change over time.

The abovementioned method will be discussed further in details as separate model parameters.

Data acquisition parameters

- **The mesh grid**

The mesh was designed in a manner that accommodates a buffer zone from both ends of the traverse. The buffer zone was allowed to be a space equivalent to two electrodes from each end. This amounted to four cells on each side. Since the study used 49 electrodes, the mesh consisted of 98 cells. The vertical cells amounted to 17 of which the first 11 were of equal size and the rest increased with depth (Figure 15). The whole grid amounted to 1802 cells.

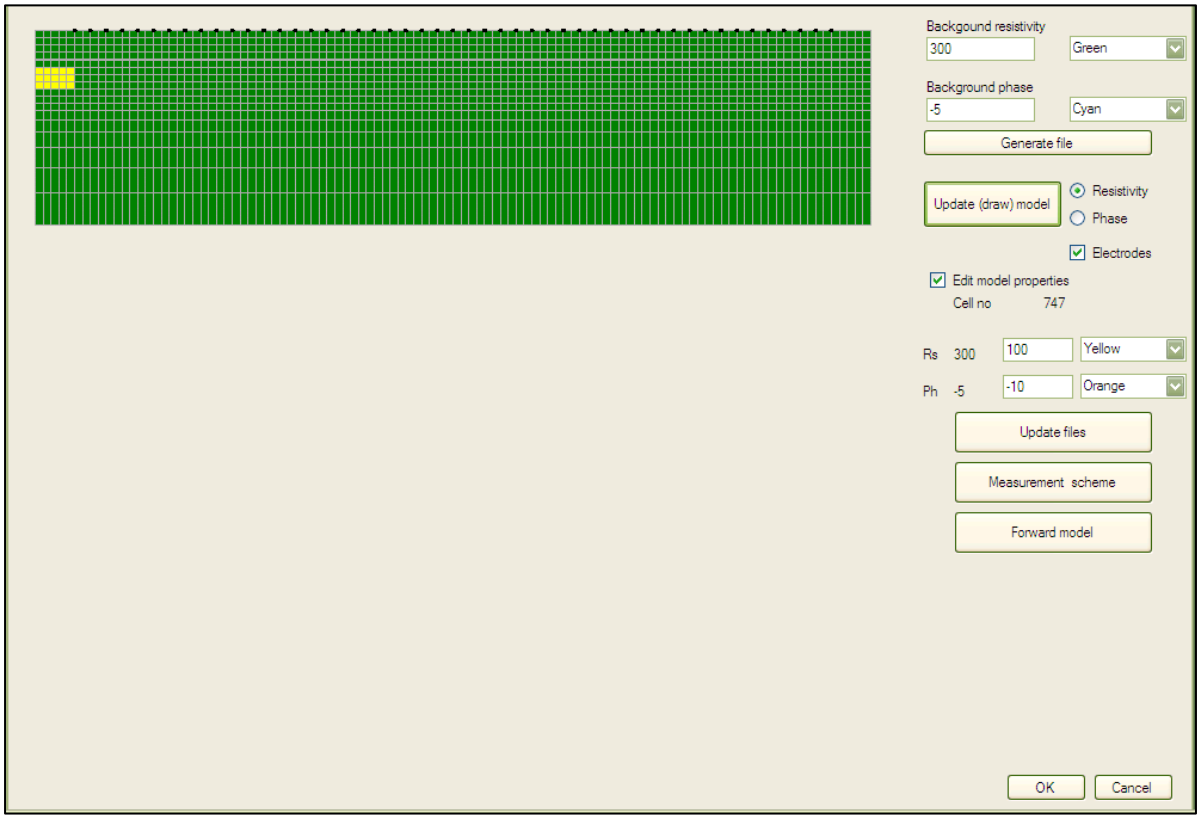

Figure 15: The CRMod used a background resistivity of 300 Ωm and 150 Ωm that remained unchanged throughout the modelling process. The black dots on top of the grid represent electrodes and the yellow blocks represent the change in resistivity which varies from 10 Ωm to 45 Ωm.

- **Electrodes addition and configuration**

A total of 49 electrodes were used in the model over the length of 288 meter traverse and the multi-gradient array was the configuration of choice. The use of multi-gradient has been justified earlier in the methodology. Resistivity values that are equivalent to the ones of the field geology are used.

- **Forward model calculation**

An internally developed CSIR programme named CRSIM was used to calculate the forward model in order to produce the data. The produced uncontaminated data were then transferred into an Excel spreadsheet where the 2% random Gaussian noise was generated per individual cell. The chosen noise level was in line with the amount of noise experienced

in the field. The instrument used in the field has the power to detect the level of sensitivity of which studies have assumed it to be 0.1 Ωm (Van Schoor, 2009).

- **Inversion**

The data from the forward model are then used in the inverse process to produce the final image which is used for assessments. The final image produces the resistance values which are used in calculating the resistance difference in the time-lapse process. Each model runs for an average of 40 minutes until the iteration process is completed. Every inversion results in different resistance values.

5. MODEL STUDY

5.1. Study approach

The WRC project on which this study piggy-back, aims to determine the progression of aquifer pollution over time by using time-lapse ERT. The purpose of this model study is to assess the performance and the limitations of the time-lapse ERT approach. A number of simplified baseline geoelectric model scenarios will be considered. For each model, the resistance value of the aquifer target is adjusted to simulate changes over time. Various levels of changes are considered, ranging from a large change (ratio of target resistance in baseline model compared to change model by a factor of 5) to a very subtle change (change ratio of 1.1). By comparing the different change model results with the baseline model results, it is possible to gauge whether such changes could be detected in principle.

5.2. Baseline geoelectric models

A number of apparent resistivity models depicting different subsurface scenarios were used as the baseline for this study. The models are as follows (refer to Figure 16). The first model (Model 1a) is a three-layered Earth scenario in which the more conductive middle layer represents a weathered saturated dolomite layer. This layer is sandwiched between a 12 m thick, more resistive unsaturated overburden layer and an unweathered dolomite basement layer at the depth of 27 m below the surface, presumed to be more resistive than the middle layer. The upper layer was assigned a resistivity of 300 Ωm, 50 Ωm for the middle layer and 150 Ωm for the basement layer. The second model (Model 2a) represents a wedged-shaped zone of contamination with a resistivity of 50 Ωm penetrating the unsaturated 300 Ωm overburden and the basement layer of 150 Ωm. The third model (Model 3a) represents a thin vertical grike that has a resistivity of 50 Ωm going through a 300 Ωm overburden to the 150 Ωm dolomite basement layer. The fourth model (Model 4a) represents a cavity located between the overburden and the basement layer. The cavity, which is assumed to be water-filled, has a resistivity of 50 Ωm. The fifth model (Model 5a) is similar to the first model (Model 1a) but Model 5a has a thinner layer (9 m versus 21 m in Model 1a). Model 6a represents a dipping grike with similar characteristics as Model 3a and the last model represent a 21 m overburden over a basal saturated layer (Model 7a)

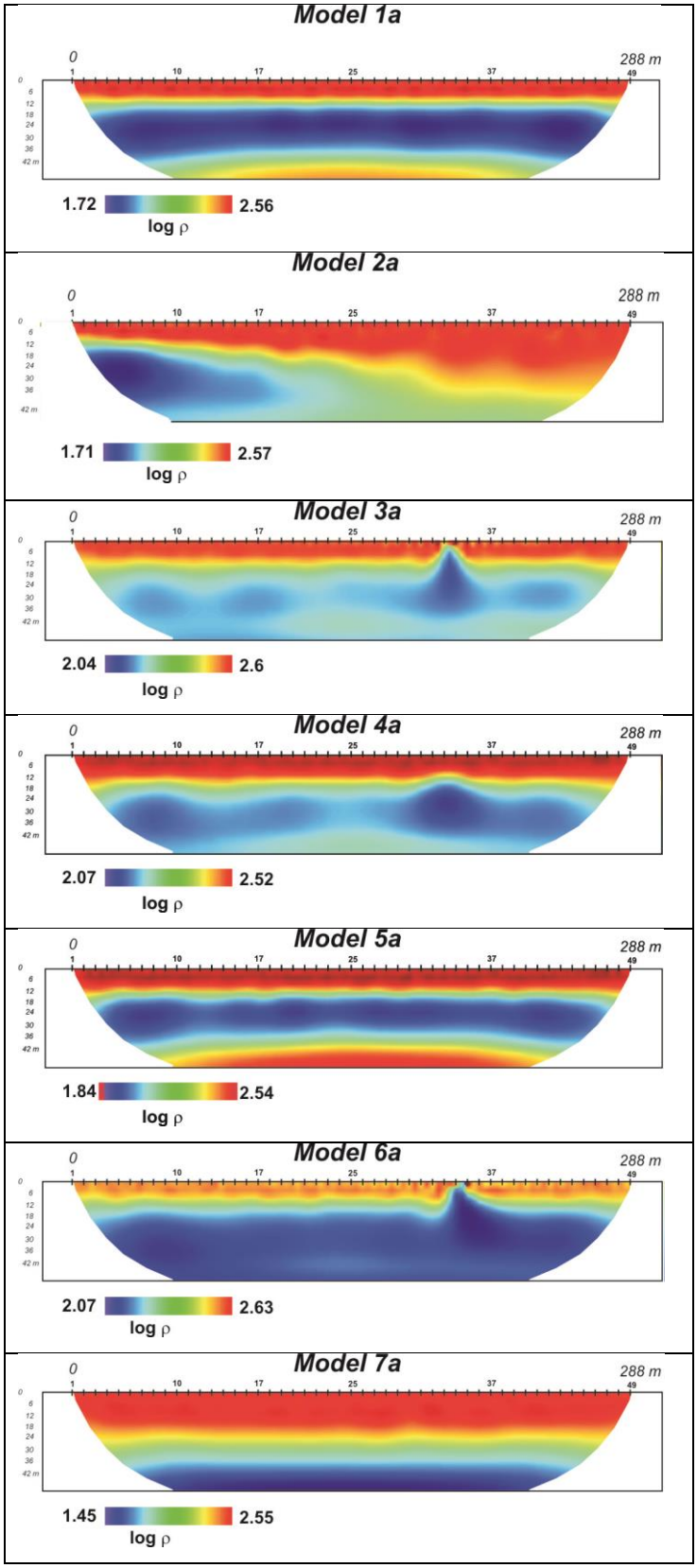

Figure 16: Baseline images depict the calculated resistivity modelled scenarios with model 1-7 representing the following; 1)Thick aquifer, 2) wedge shaped contamination zone, 3) a vertical cavity,4) a cavity, 5) a thin lateral layer, 6) a dipping cavity and 7) the overburden over saturated layer.

5.3. Model change specifications

The field responses and corresponding inversion outputs were calculated using CRmod and CRTomo. The difference change in resistance is assessed against the baseline model for each of the five different change models. The same procedure was repeated for each of the baseline model scenarios, as summarised in Table 1.

Table 1: Model change specifications are provided as variations of the pollution plume overtime in order to detect threshold of which the lowest difference in resistivity could be detected. The target layer resistivity varies from big differences (10 Ωm) to very subtle differences (45 Ωm).

Model Number	Target layer resistivity	Ratio of target layer resistivity to the baseline model
A	50	-
B	10	1: 5
C	16.7	1: 3
D	25	1: 2
E	33.3	1: 1.1.5
F	41.7	1: 1.2
G	45	1: 1.1

Note: Table 1 above indicates the applied changes for all the models from A to G.

5.4. Results

The inverted models that represent the various transient change possibilities are compared against the baseline images in Figure 17.

Model 1

Figure 17 shows the inversion output for Model 1a that represents the baseline model as well as the results for Model 1b to Model 1g, which represent possible survey results for the same survey as in Model 1a but at some point later in time. The model variation outputs are then compared against the base models.

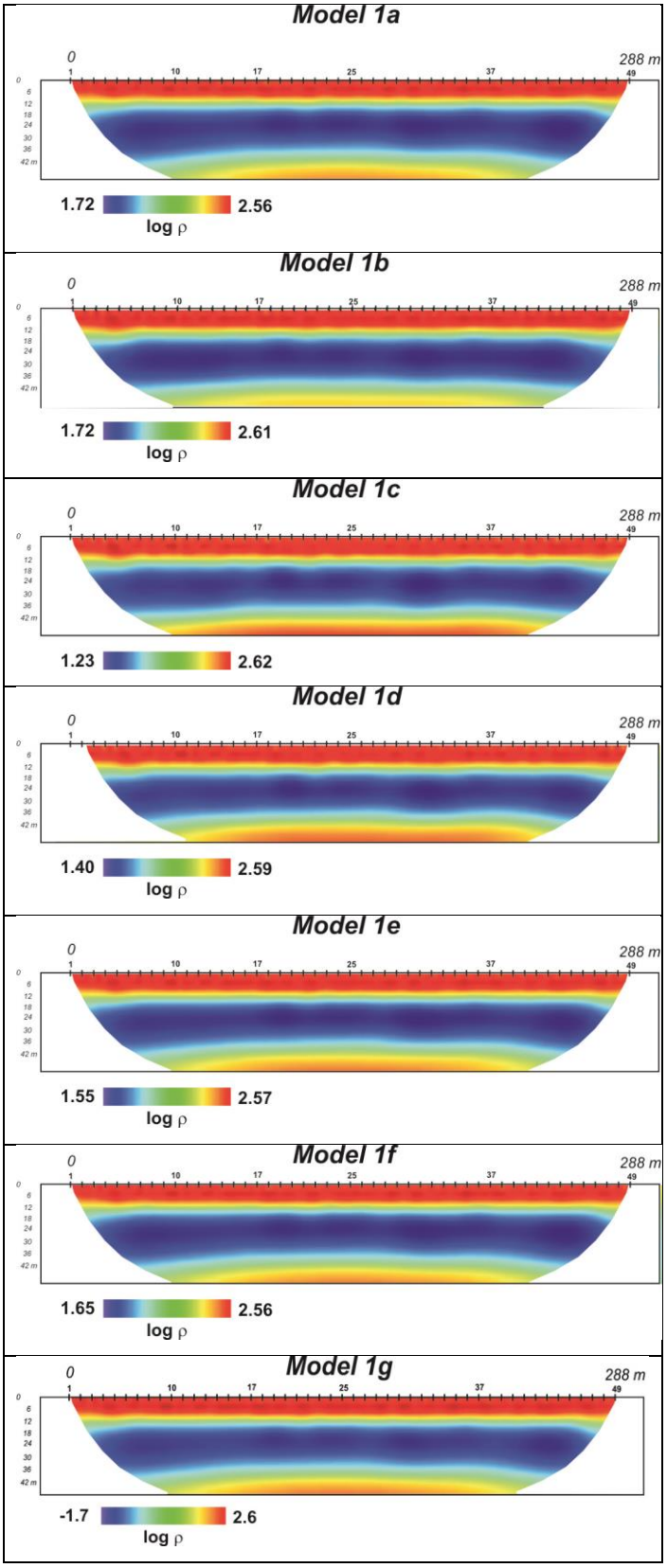

Figure 17: Model 1 inversion output images shown should be depicting the images but this can only not be clearly visible since the equivalents adjust according to the changes is resistivity. Difference images are more visible because they focus on the difference in the image.

A common way of plotting resistance images is to use the actual image limits when selecting a colour bar for display. This approach was used to produce the images in Figure 17. It is noteworthy that it is not easy to discern the differences between any of the images between Models 1b to Model 1g when compared to Model 1a. The image limits shown below the colour bar provide the indication that the image range is narrowing from Model 1b (large change) to Model 1g (small change). However, the image limits cannot be used as a reliable measure of change as outliers in the inverted image could complicate such analysis. In other words, while the image limits simply reflect the absolute pixel value extremes, for the purpose of detecting subtle changes, it would be better to consider the overall distribution of the pixel values.

Another way of representing repeat survey outputs is to assign the same image limits used to display the baseline image. This approach is demonstrated in Figure 18 where the images from Model 1br to Model 1gr are all plotted using the same image limits that were calculated for Model 1a. It is clear that the changes in aquifer resistance can be inferred by comparing different model outputs such as Model 1br against that of Model 1a. The large change in the aquifer resistance (1:5) manifests as much more prominent (darker blue) apparent layer when compared to image 1a. However, as the change in aquifer characteristic becomes more subtle, it becomes increasingly difficult to visually discern the change. This can be seen when comparing Model 1fr and Model 1gr with that of Model 1a.

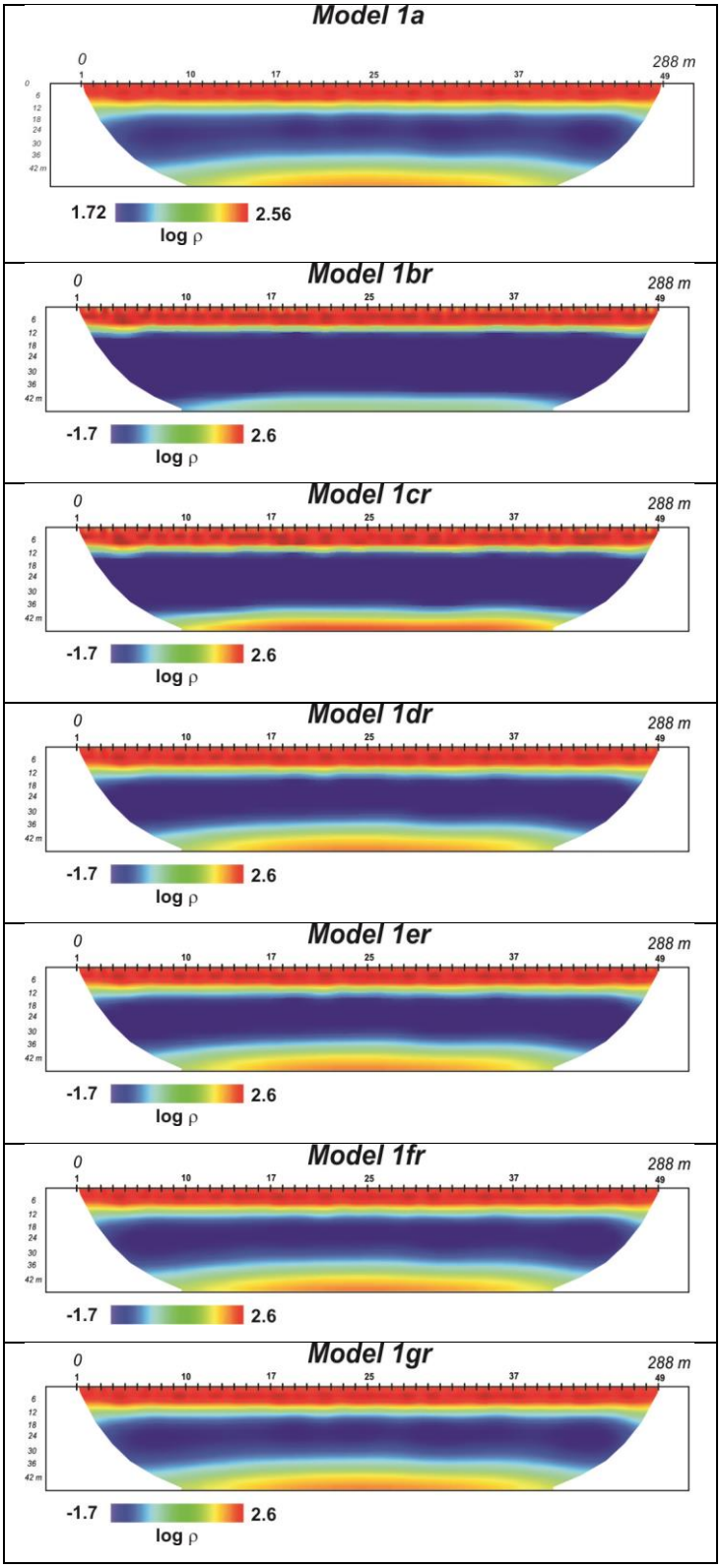

Figure 18: Model 1 Inversion image outputs using constant limits show clearer differences in the output images between the extreme changes but do not show as much difference as the difference images in Figure 19. The image differences are more visible in Figure 18 than in Figure 17 because of the relative image limits that are used in Figure 18 rather than actual image limits used in Figure 17.

The approach to detecting transient changes in resistivity that is used in this study is that of difference imaging. This involves calculating the difference between repeat surveys and the baseline survey pixel values, and representing the difference as percentage change images. This approach is demonstrated in Figure 19. These difference images are displayed using the actual absolute difference image limits in each case. In other words, if the absolute maximum change in a difference image (positive or negative) equals say x, the image limits used for display purposes is then ± x%. This is to avoid biasing positive or negative changes. Figure 19 shows the difference images for the various Model 1 change possibilities calculated in this way.

The main advantage of the difference approach is that its supresses the resistance features that do not change over that time between the baseline and repeat surveys while emphasizing those parts in the survey areas that do change. This effect is evident in Figure 19. Only the change in the middle layer (aquifer) resistance stands out as an 'apparent anomaly'. The change can now be easily inferred (visually) even for very subtle changes, for example, in difference Model 1af and Model 1ag shown in Figure 19. Even though it may appear that the difference approach performs equally well for large and very small changes, this is actually not the case as can be seen in the narrowing of the percentage change range. For example, in the case of the biggest change, the range on the difference image is almost 40% while the value of the smallest change is only about 2%.

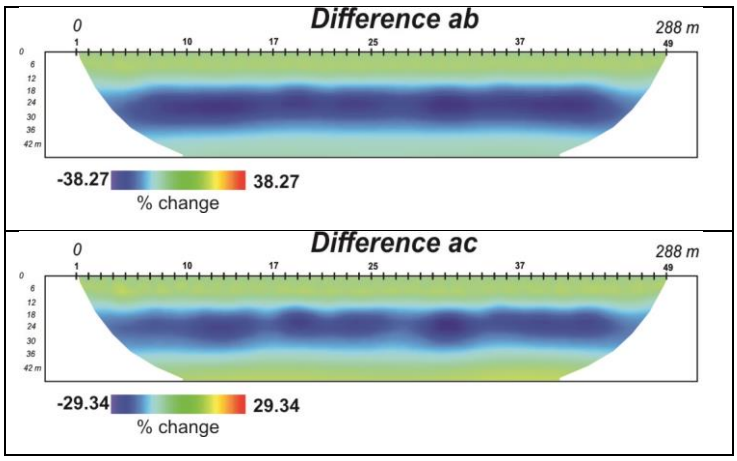

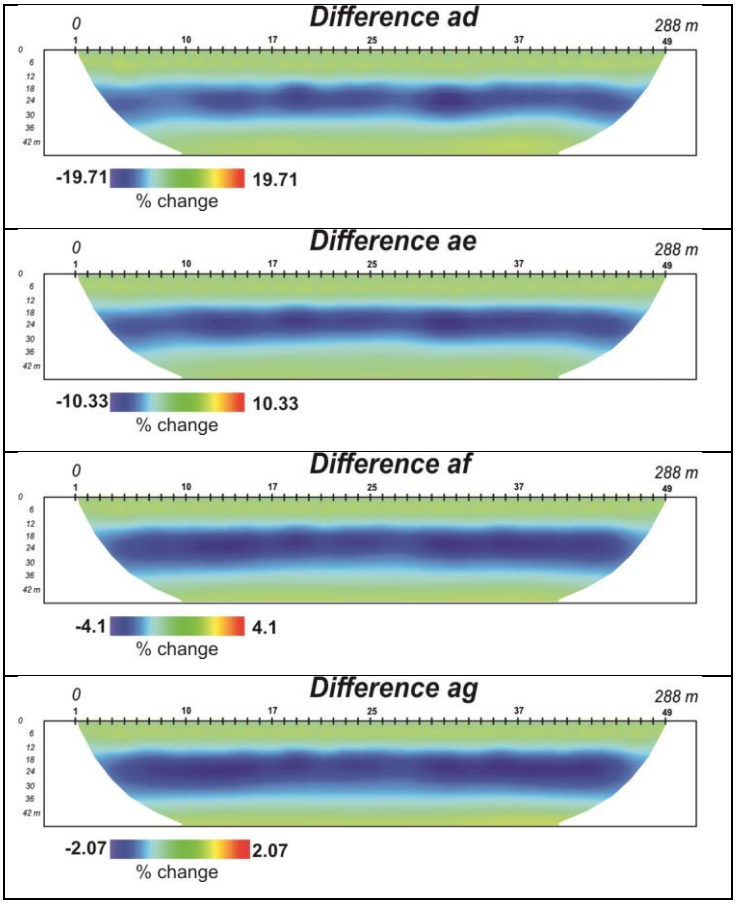

Figure 19: Model 1 difference images show the change in the size if the aquifer due to change in model sensitivity. Difference ab, ac and ad show higher contrasts to the base model because of the large difference in their resistance.

Model 2

A similar processing sequence reported for Model 1 (Figure 19) is applied to Model 2 is shown in Figure 20. Figure 20 and 21 show the inversion outputs for baseline surveys for Model 2 and a range of possible repeat survey scenarios. Figure 20 shows the results using the actual image limits which results in similar images, while Figure 21 uses the relative image limits (as before by using the baseline image limits) which shows the differences in images. The same observations noted for Model 1 also apply here.

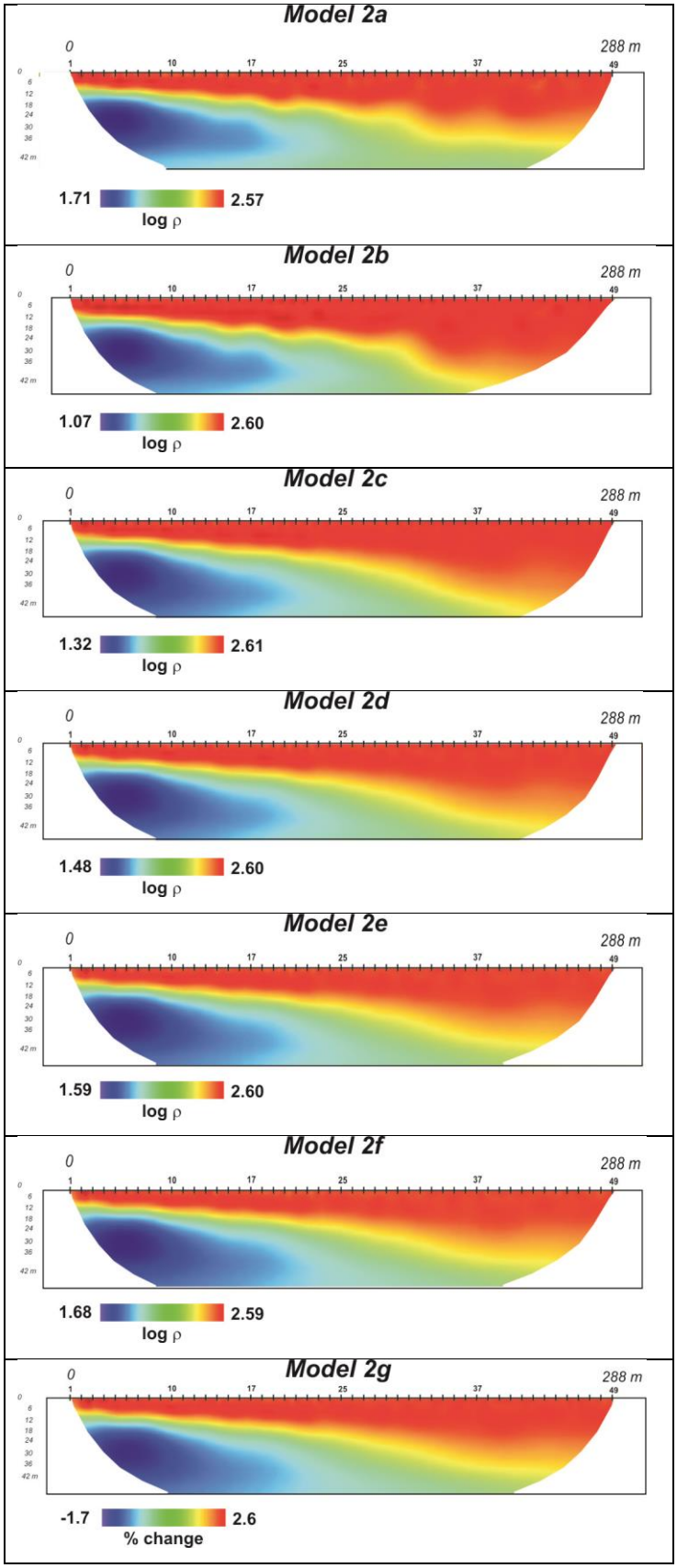

Figure 20: Model 2 inversion images uses actual image limits which results in no difference in outputs images since the limits are adjusted according to the observed image diference.

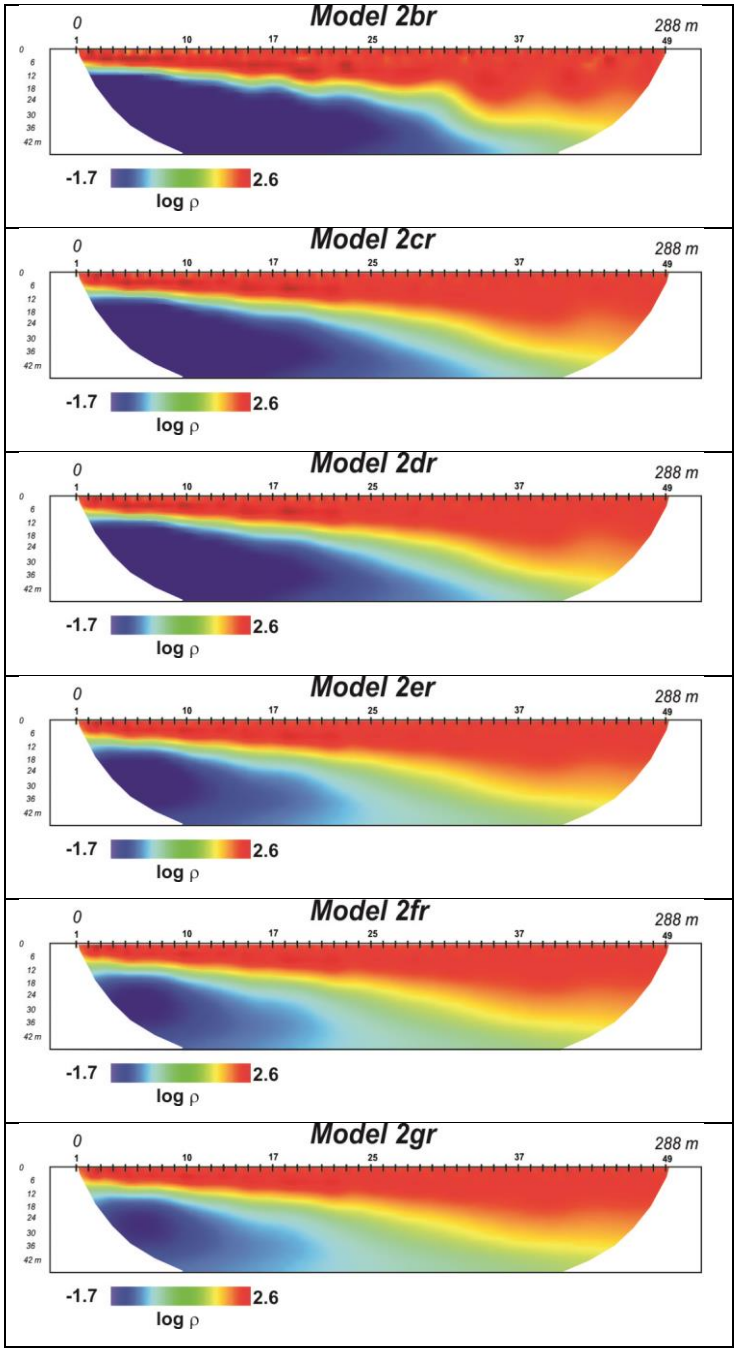

Figure 21: Inversion images with relative image limits depict a more visible change in the models as the resistivity levels change. Constant limits allow the visibility of distortions in images.

Figure 22 shows the difference image results according to the changes shown in Table 1 and are calculated in the same way as for Model 1 in Figure 19. However, a significant difference in the performance of the difference imaging approach is immediately apparent as shown in Table 1. As the percentage change range narrows, the image quality deteriorates

and becomes characterised by noise and distortions of the anomalous zone. This deterioration in image quality can be attributed to the fact that the percentage change values approach the same order of magnitude as the noise in the data. The reason this phenomenon is observed for Model 2 but not for model 1 is thought to be related to the different model geometries.

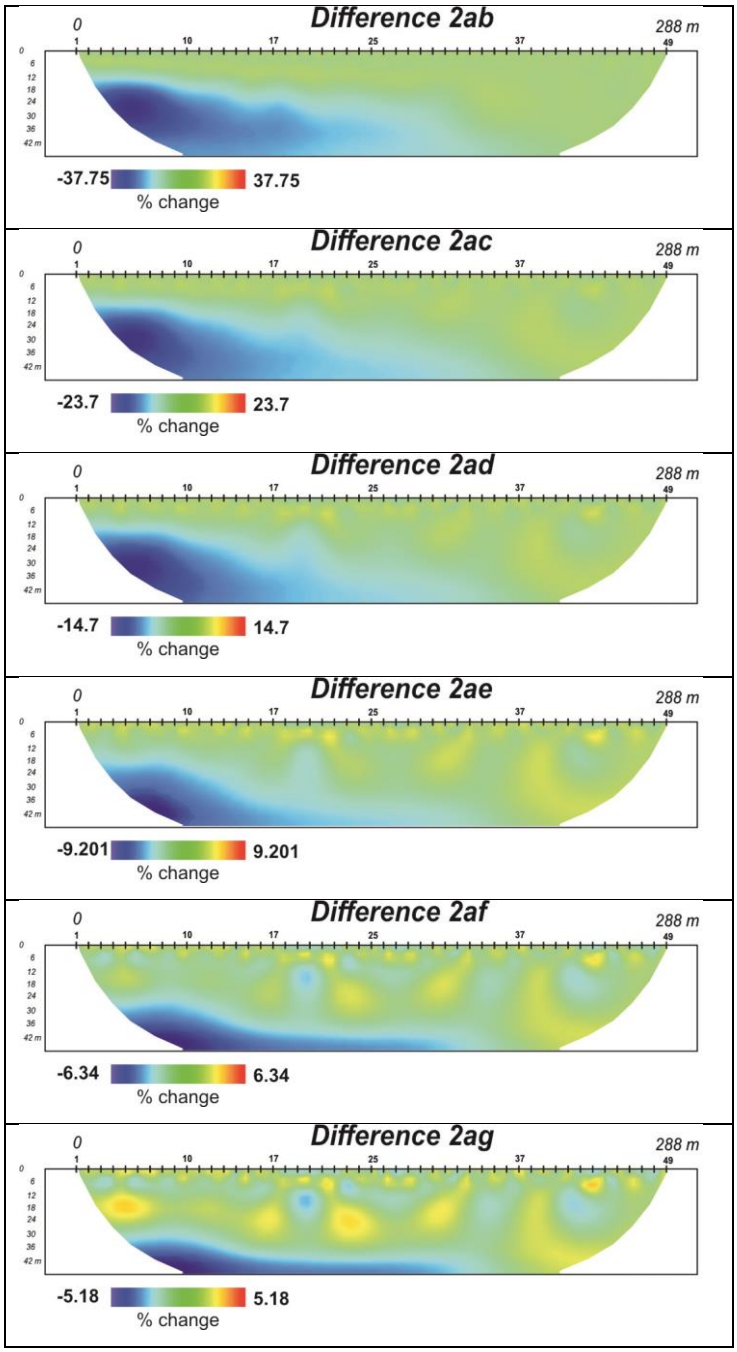

Figure 22: Model 2 difference images output show a localised contamination portion of the aquifer and the output changes as the resistance is reduced between the final model and the base model. Artefact and distortions take effect at Difference 2ad because of the position of the pollutant.

The aquifer layer in Model 1 represents a much more favourable target than the wedge shaped Model 2 because of its relatively greater size and lateral extent. This can also be explained by the fact that the electrode configuration (multi-gradient array) and measurement scheme used is much more sensitive to the relatively thick layered aquifer with lateral extent across the whole survey area, compared to the smaller, localised wedge target. Furthermore, the wedge shape is located close to the boundary of the grid which is a low sensitivity area for the ERT method (Figure 14).

Model 3

In presenting the results for Model 3, a similar approach has been used as in the previous two models, with the exception that the relative images are not included. The use of actual image limits in Model 3 in Figure 23 indicates the change in grike resistance overtime according to Table 1 resistivity changes. The change in visibility of the grike is only apparent at the larger resistance changes (Model 3b to 3e). For more subtle changes the output resembles the baseline model output. The difference models clearly detect the transient changes overtime as shown in Figure 23.

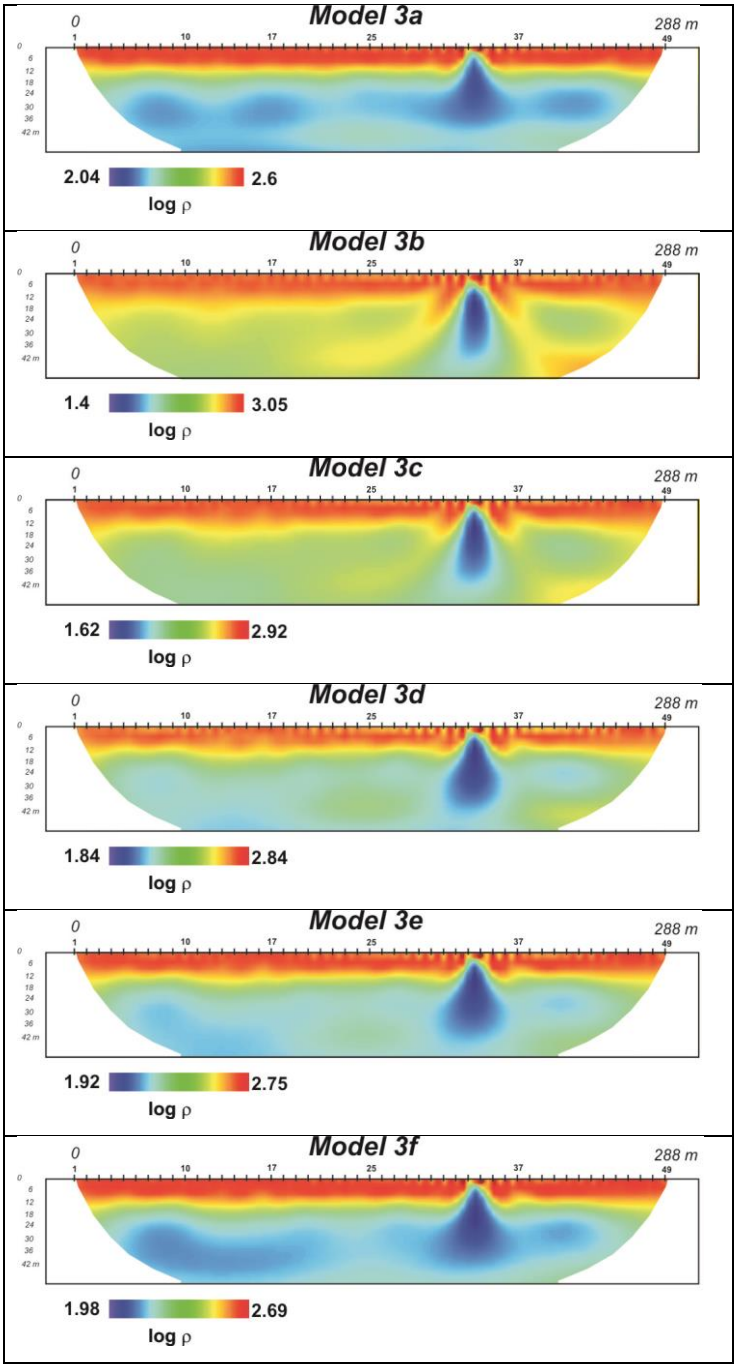

Figure 23: Model 3 inversion image outputs depicts a grike that is visible at higher resistance differences such as Model 3b and 3c. The less different inversion outputs (Model 3c to 3e) are also slightly differentiable from base image (Model 3a) and not differentiable (Model 3f) due to the least change in the resistivity differences.

The increase in distortions is again observed as the change in percentage difference (Table 1) decreases (Figure 24). The target geometry most likely plays a role in the imaging (and difference imaging) performance. The grike target is a narrow vertical structure with a width of only half a unit of electrode spacing. Also, the grike is vertical and so the horizontal

resolution is not extremely sensitive to the limited lateral extent of this target. Hence the dominance of artefacts in subtle resistance difference which can be seen for the smaller resistance changes in Difference 3af and Difference 3ag.

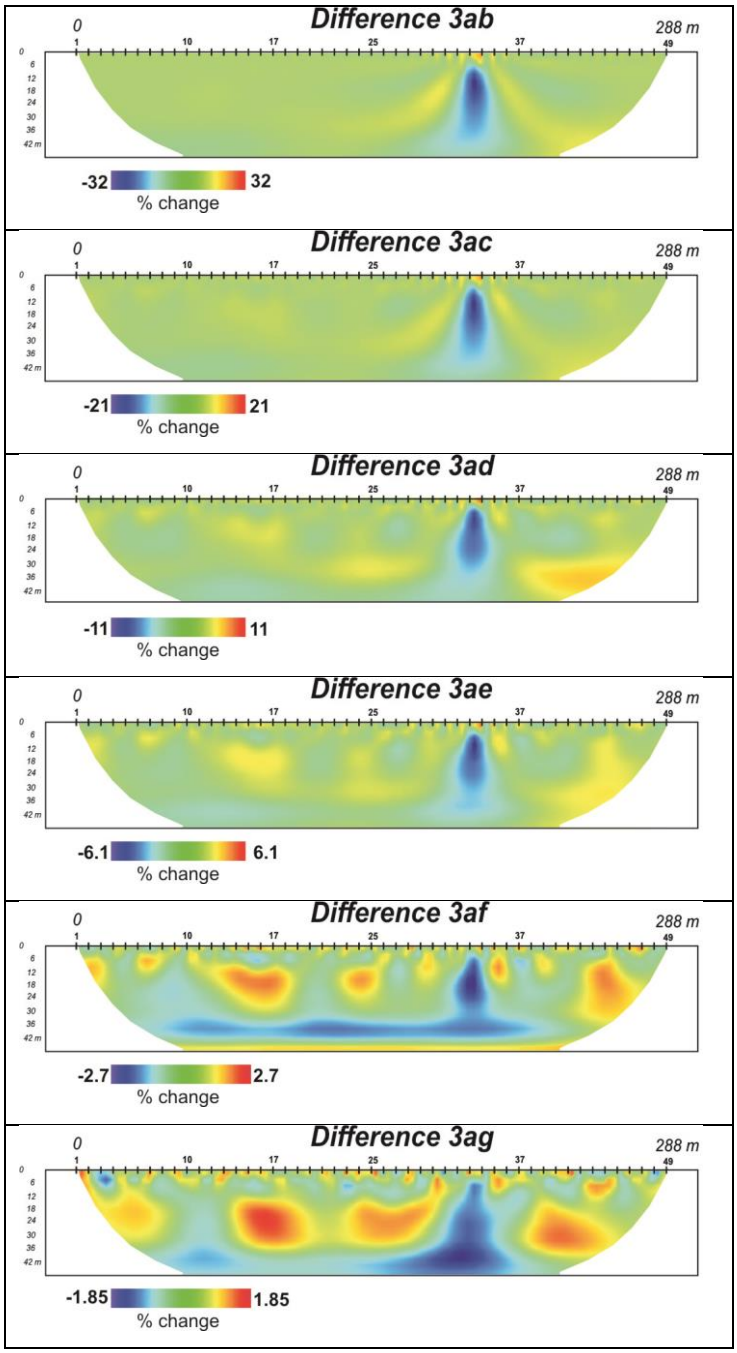

Figure 24: Model 3 difference images show the impact of background noise as the resistivity difference is reduced to an extent that it distorts the target point. The difference output images keep the target point until the resistivity difference is at 10% (Difference 3ag) where more background effects become visible. However, the target remains visible despite the distortions.

Model 4

For Model 4 (Figure 25), the data representation approach used is the same as the one applied in the previous model results. The actual inversion images show the change in resistance over time as shown in Table 1 when comparing only the extremes, but not the subtle changes. A cavity is the target for this model and even though it is also a small localised target like the grike model target, it has a lateral extent which is three times longer. This slightly more favourable target geometry results in the corresponding difference imaging performing better than for the grike. It can be seen in the difference imaging shown in in Figure 26. The distortions also become visible as the resistivity difference becomes smaller at difference 4ag in Figure 26.

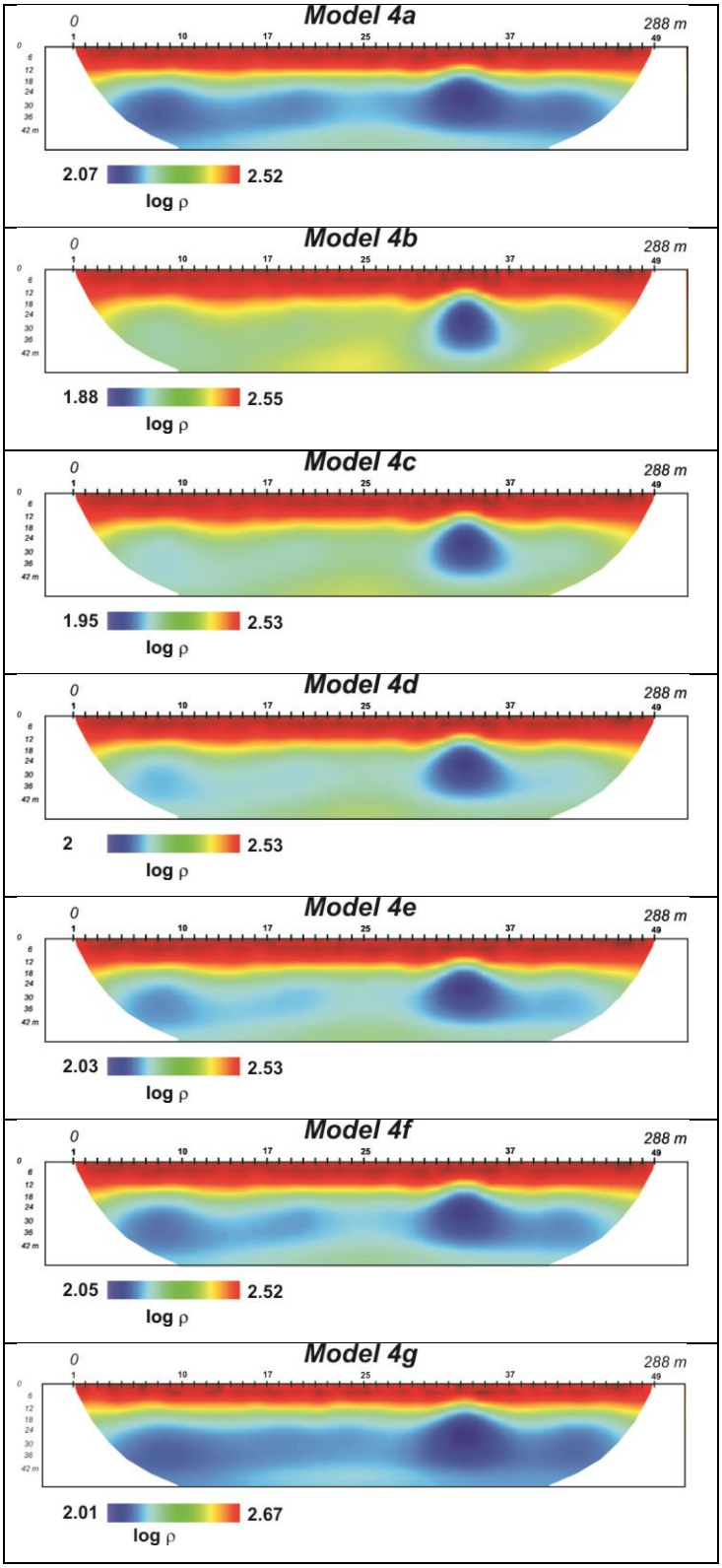

Figure 25: The inversion results for the modelled cavity Model 4 show that the difference in inversion images is clear at extreme differences such as Model 4b, c and d against a. Model 4g with the most subtle change of resistance against the base model also shows differences.

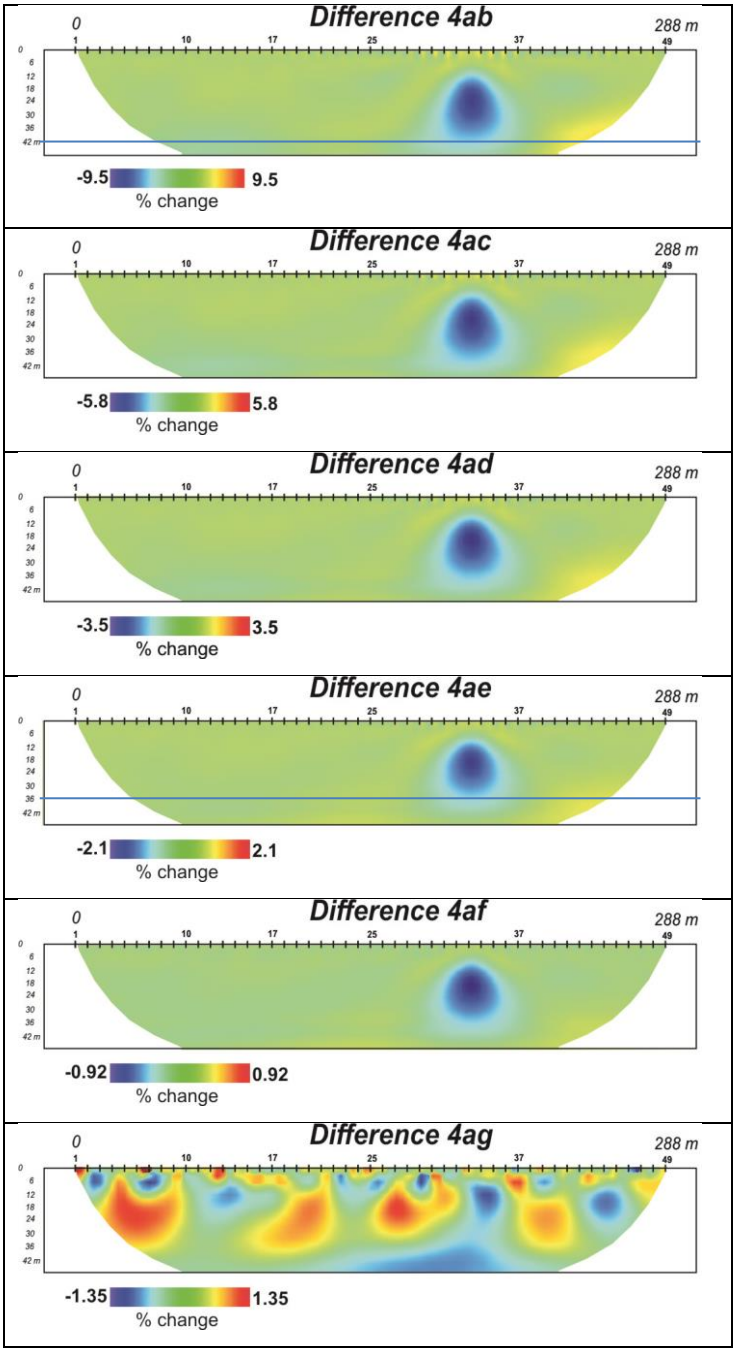

Figure 26: Model 4 difference image output show the high detectability of the target until Difference 4ag where the background noise interferes. Difference 4ab to 4af are almost similar but the target gets distorted from the bottom as (Difference 4ab at 42 m against Difference 4ae at 36 m) the resistance difference becomes more subtle to the baseline image.

Model 5

The results for Model 5 represent a thin lateral low resistivity layer (Figure 27). The thickness of the target makes it visually impossible to discern the resistivity differences in between the inversion images. Further application of difference models assist in differentiating the change in resistance levels between the models over different timeframes.

The difference models (Figure 28) focus on emphasizing the changing properties of the aquifer. Here the change in the thinner middle layer (compared to Model 1) is detected in all cases except for the most subtle changes (Difference 5ag). The fact that the difference approach fails here and not in the case of Model 1 is attributed to the fact that the much thinner target layer is represented as more challenging because the electrode configuration wouldn't able to easily detect the target because of its thickness.

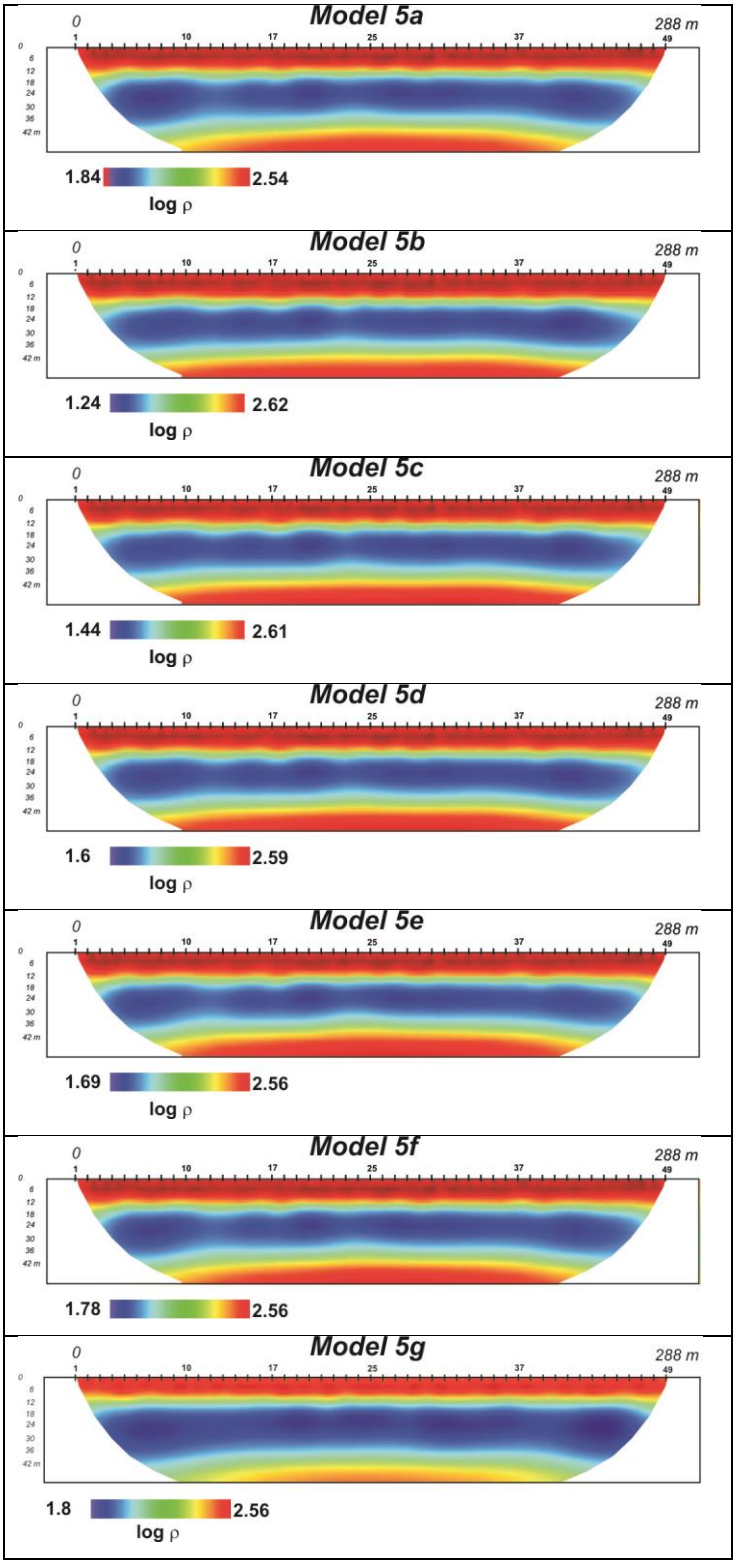

Figure 27: Model 5 inversion images show the thin lateral low resistance layer. It is similar to Model 1 but Model 5 difference cannot be discerned because it is too thin.

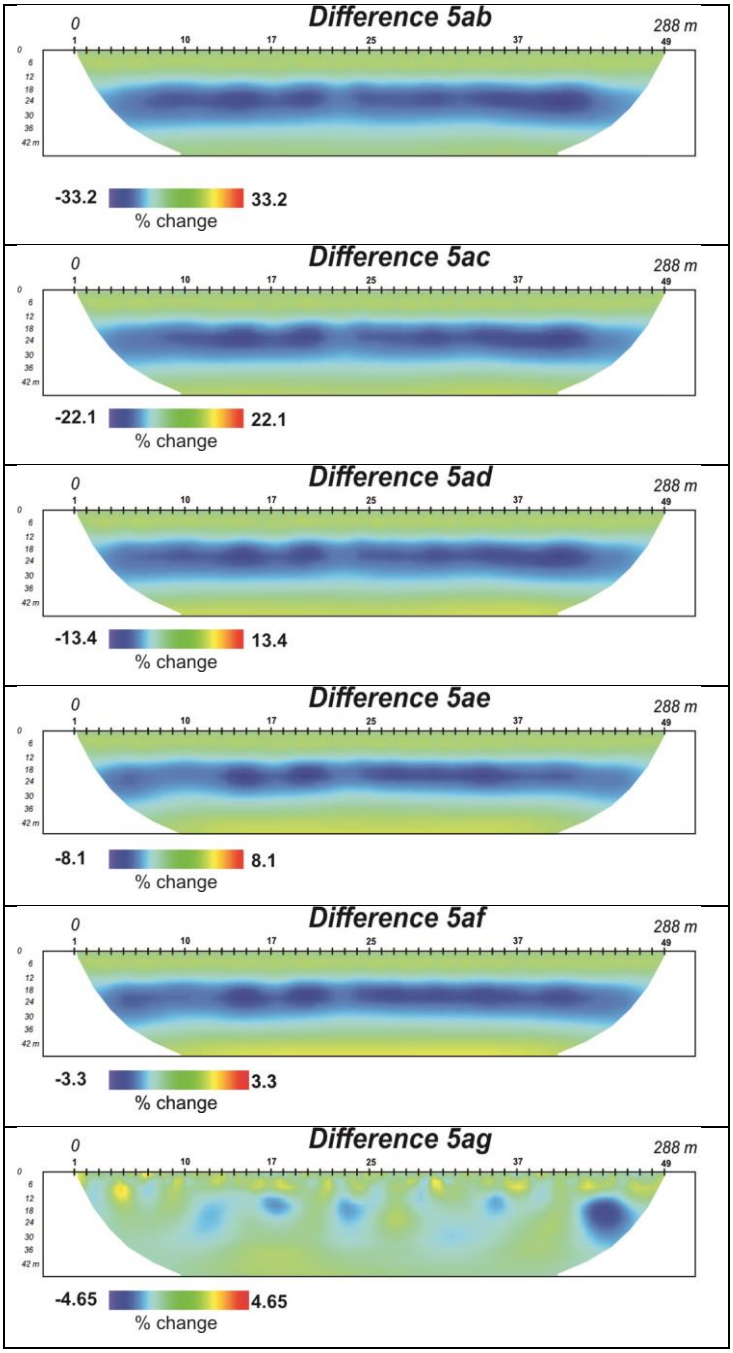

Figure 28: Model 5 difference image outputs show that the target is detectable until the smallest difference level (Difference 5ag) is reached where the background artefacts start distorting the image.

Model 6

Figure 29 shows the inversion results for the transient changes (as shown in Table 1) in the properties of a dipping grike. The inversion model results (Figure 29) reveal the evidence of the resistance changes for Models b, c and d. However, for more subtle changes the images appear very similar to the baseline image (Model 6a). The artefacts are only visible when

applying the difference changes against the inversion images and this is observed in Figure 30.

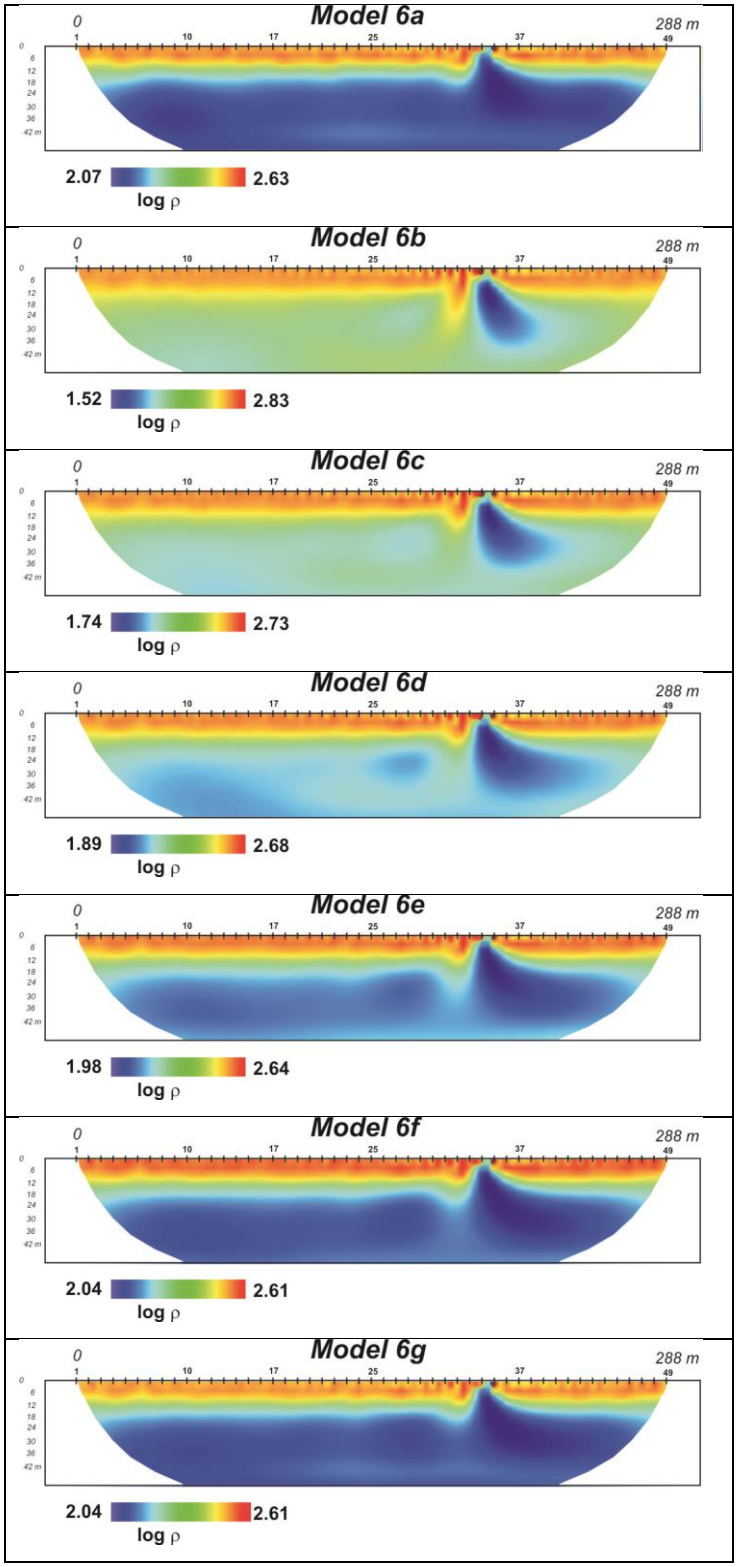

Figure 29: Model 6 inversion image outputs shows a dipping grike that is detectable at high to subtle changes (Model 6b to 6d).

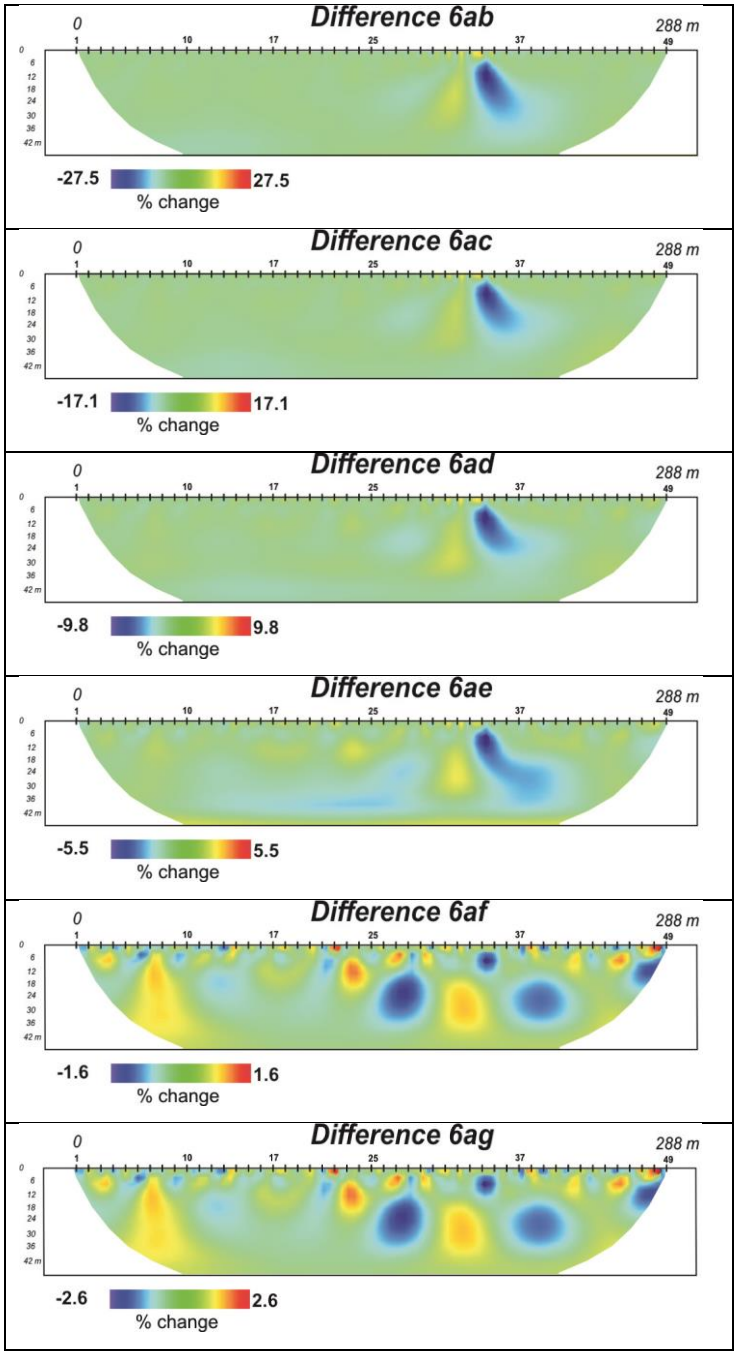

Figure 30: Model 6 shows difference images of a dipping grike that has higher background impact to the output image at lower resistivity difference (Difference 6ae) to the base image and dominate the image at Difference 6ag.

The difference images in Figure 30, as with other difference images above, clearly indicate the transient resistance changes of the target areas. The dipping grike becomes more visible than the vertical grike in Figure 23 due to the geometry of the dipping grike model (Lateral

extent) and the electrode configuration chosen, which allows more lateral sensitivity. However, the shape and visibility of the target gets distorted at low ratios such as in Figure 30 (Difference 6ag). High distortion levels are reached when the image differences are of the same order as the noise levels 2% used in this study.

Model 7

Figure 31 models a 21 m overburden layer of 300 Ω) lies over a basal saturated layer. The inversion models do not reveal any difference that is visible. However the difference images in Figure 32 clearly show the actual difference.

The difference models shown in Figure 32 indicate that the change in the aquifer resistance difference is visible even at the most subtle resistance difference (Difference 7af and Difference 7ag). Although there is some form of distortion, the target point remains visible. This distortion may be due to the greater thickness of the layer (compared to the middle layer in Model 1) which lies in a low sensitivity zone.

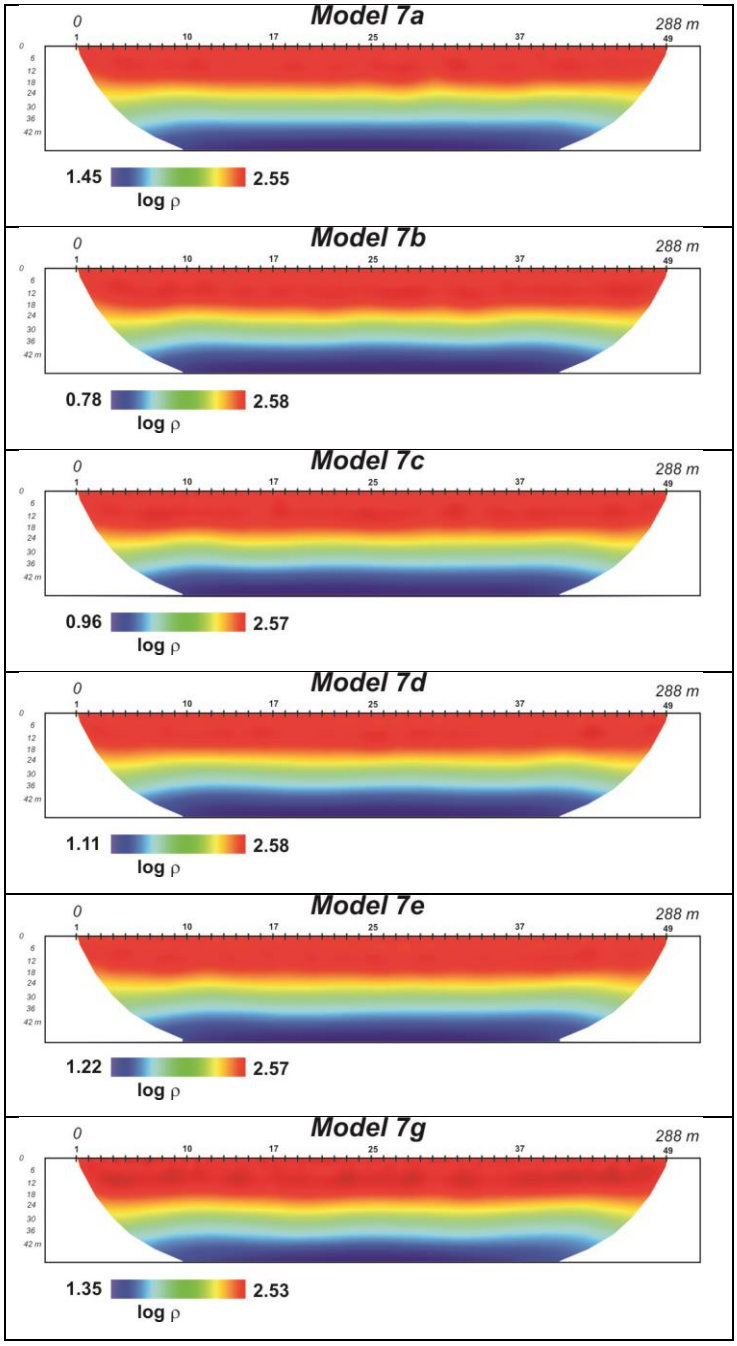

Figure 31: Model 7 inversion images outputs show overburden over low resistive saturated medium. The inversion images are not easy to discern and the difference method is applied to detect the difference in resistance.

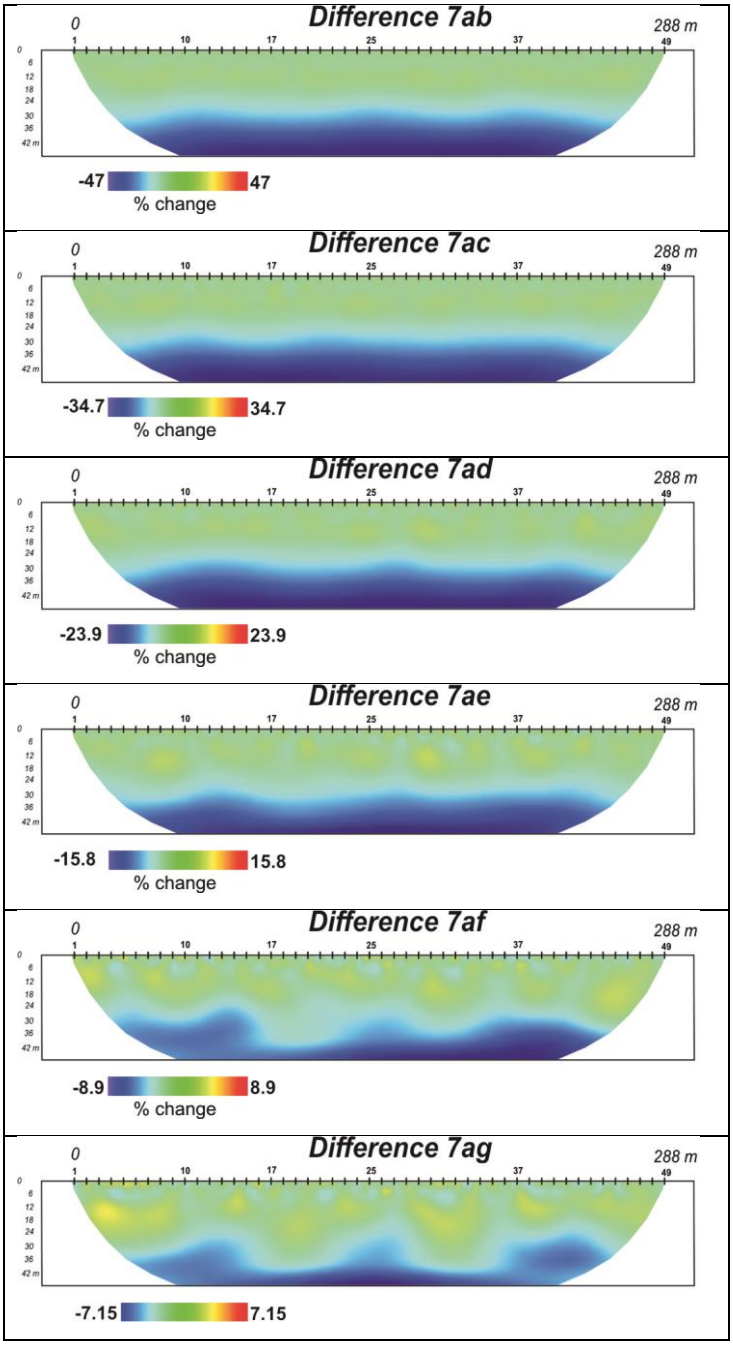

Figure 32: Model 7 difference images show the results the overburden that gets distorted by the artefacts at higher resistivity differences (Difference 7ae) than other in other model images. However, the smallest difference remains at Difference 7ag remains visible even though it gets distorted as the background effects take place.

5.5. Discussion

The inversion images from the models indicated that transient changes can be discerned, to a certain extent, by directly comparing the original (baseline) and subsequent (repeat) survey outputs but this depends on geoelectric properties.

The difference approach performs generally well, but for the more challenging scenarios – that is, subtle changes in resistance and small targets that are located in low sensitivity parts of the survey area - it may fail. The failure is characterised by distortions of the target area and the dominance of unwanted noise related artefacts which come into play as the level of sensitivity towards resistivity decreases. The best targets for the type of pollution monitoring that is attempted in the WRC project would be thick layered aquifers or basal layers that are located relatively close to surface; that is the top of the aquifer should not be so deep that it lies in a low sensitivity zone. The accumulated sensitivity images (Figure 14) can be used to determine the applicability or to optimise the electrode configuration in this regard.

The modelling software (CRTomo) used in the study allows for the modelling of the karst environments and also limits the noise level to 2%. The modelling of 7 scenarios at 7 different resistivity levels per scenario allowed the detection of the models' strengths and weaknesses, which further indicated the ideal applicability in the real geological conditions. Inversion model images could not be used in isolation as they could not discern minimal differences and the visibility of artefacts that distorted the target rockets. However, the use of difference images was ideal since they only emphasized the changing characteristics about aquifer and could clearly detect the impact of noise.

The electrode configuration chosen in the model study is more sensitive towards the lateral variations of the aquifer (profiling). This was identified through the detection of lateral transient changes that were still visible even at the smallest resistance changes. The model parameters can be regarded as lenient towards central, lateral and large targets. On the other hand, vertical, sub-vertical and small targets such as grikes and small cavities are easily distorted by background noise. In addition, thin lateral structures are also distorted by background noise at much higher resistance differences (Difference 5af) in Figure 28 than the bulky targets (Difference 1ag) in Figure 19.

The electrode configuration sensitivity weakens towards the edges of the model result in strictures such as the wedged model (Figure 22) becoming distorted at the smallest resistivity resistance change (Difference 2af and ag). The distortion applies regardless of the size of the wedge because of its position in the model. On the other hand, thick lateral

structures (Difference 1ag and 7ag) in Figure 19 and 32 are still more prominent even at the most subtle resistance changes against their respective baseline models.

The modelled grikes of similar width but different orientations (vertical and dipping) also show different outputs at their most small resistivity difference levels against their respective baseline models (Figure 24 and 30). Difference Model 3 (Figure 24) indicates that the artefacts start interfering with the model at higher resistance difference (Difference 3 ad) while the same artefacts on Figure 30 become effective at more subtle resistance differences (Difference 6af). This may be attributed to the chosen electrode array that is sensitive to lateral variations since their width is the same. The sensitivity of the configuration is also observed in Model 4 difference (Figure 25) and Model 5 difference (Figure 27) image resistance variations where the electrode configuration is sensitive on both images until the most subtle differences (Difference 5ag and 4 ag). The detection of a thin lateral target with the least resistivity difference to the base model becomes a challenge because of its small thickness. The cavity (Figure 26) becomes impacted by artefacts at much smaller resistance difference (Difference 4ag) than the thin lateral layer of Model 5 (Difference 5ae) on the other hand remains visible because of its large larger size.

The model difference outputs may not be perfect it has the ability to determine the target at differences as low as 10% when using a single configuration of which was the multi-gradient array in this study. This goes to show that more data without distortions can be produced at lower resistivity differences, provided the target is known and the configuration is suitable for the survey.

The obtained results indicate that there is still more improvement that is required within the field of geoelectric modelling due to the level of distortions at low resistivity differences but the results also indicate that, similar to field work, the results will be obtained according to the sensitivity of the configuration used, hence the modelling potential to drastically reduce the time that is spent in conducting the actual fieldwork in the near future.

6. CONCLUSION AND RECOMMENDATION

6.1. Conclusion

Abandoned mining operations from the vicinity of COH WHS have resulted in the generation of AMD, which has potential catastrophic impact on water resources if not carefully monitored. The monitoring methods that have been put in place have proven to be ideal in obtaining quantitative data; the current methods involve drilling and sampling and analysis of water. However, such monitoring methods are costly and time consuming to execute. The use of time-lapse electrical resistivity surveys provides an alternative monitoring method that can supplement the drilling and sampling approach

This study focused on modelling typical field scenarios using time-lapse ERT survey approach. The simulation or forward modelling process uses assumed realistic field parameters as a reference in order to produce synthetic survey results that would match actual field survey result.

It can be stated, following the model study presented here, that the time-lapse ERT modelling can be applied to karstic aquifers since it has the potential to detect very small transient acidity changes. However, the time-lapse approach may fail if the change is very subtle and the target geometry is unfavourable. Unfavourable targets are relatively small (especially in the lateral sense) and/or are located in low-sensitivity zones of the survey area.

The modelling of karst aquifer scenarios using CR modelling with the chosen multi-gradient configuration indicated that targets that are closer to the surface are easier to detect than the ones at greater depths. The model matrix shows, for example, that thin vertical targets are prone to be quickly distorted by background artefacts. Similar effects apply on lateral thin targets at increasing depths because the sensitivity decreases with depth.

The hypothesis of the study was proven and this means that relatively low changes in subsurface resistivity can be detected for scenarios in which targets are considered favourable as described above. Also, such changes in subsurface resistivity can be attributed to changes in pollution levels since the other parameters that may influence resistivity are not expected to change significantly over the same period of say 1-2 years.

6.2. Recommendations

The use of CRTomo and modelling is ideal for the karstic aquifer provided the target is close to the surface because the configuration used in the model for this study is sensitive to shallow aquifers. Furthermore, geophysical modelling used in this study would be ideal if the aquifer was similar to the one modelled in model 1 but that is never the case in the real world. The correlation of actual field conditions with the model resistance subtleness would be ideal so that quantitative data can also be obtained using only geophysical modelling. This would further minimize aquifer monitoring costs as there would not be a need to physically collect the data.

It is recommended that an ongoing aquifer monitoring processes should take place in order to correlate the actual field data with those obtained from the model. This will further narrow the difference between the obtained field data and the modelled results. The success of such investigation will allow for future prediction of groundwater plume advancement and aquifer behaviour. Furthermore, more morels should be done using different arrays in order to detect their highest level of sensitivity. This can then be verified by fieldwork over the years.

REFERENCES

Agangi, A., Hofmann, A., Rollion-Bard, C., Marin-Carbonne, J., Cavalazzi, B., Large, R. and Meffre, S., 2015. Gold accumulation in the Archaean Witwatersrand Basin, South Africa—Evidence from concentrically laminated pyrite. *Earth-Science Reviews*, *140*, pp.27-53.

Aizebeokhai, A.P. and Oyeyemi, K.D., 2014. The use of the multiple-gradient array for geoelectrical resistivity and induced polarization imaging. *Journal of Applied Geophysics*, *111*, pp.364-376.

Binley, A. and Kemna, A., 2005. DC resistivity and induced polarization methods. In *Hydrogeophysics* (pp. 129-156). Springer Netherlands.

Brunet, P., Clément, R. and Bouvier, C., 2010. Monitoring soil water content and deficit using Electrical Resistivity Tomography (ERT)–A case study in the Cevennes area, France. *Journal of Hydrology*, *380*(1), pp.146-153.

Buselli, G. and Lu, K., 2001. Groundwater contamination monitoring with multichannel electrical and electromagnetic methods. *Journal of Applied Geophysics*, *48*(1), pp.11-23.

Chandra, S., Ahmed, S., Nagaiah, E., Singh, S.K. and Chandra, P.C., 2011. Geophysical exploration for lithological control of arsenic contamination in groundwater in Middle Ganga Plains, India. *Physics and Chemistry of the Earth, Parts A/B/C*, *36*(16), pp.1353-1362.

Clément, R., Descloitres, M., Günther, T., Ribolzi, O. and Legchenko, A., 2009. Influence of shallow infiltration on time-lapse ERT: Experience of advanced interpretation. *Comptes Rendus Geoscience*, *341*(10), pp.886-898.

Daher, W., Pistre, S., Kneppers, A., Bakalowicz, M. and Najem, W., 2011. Karst and artificial recharge: Theoretical and practical problems: A preliminary approach to artificial recharge assessment. *Journal of Hydrology*, *408*(3), pp.189-202.

Dahlin, T. and Zhou, B., 2006. Multiple-gradient array measurements for multichannel 2D resistivity imaging. *Near Surface Geophysics*, *4*(2), pp.113-123.

Descloitres, M., Ribolzi, O., Le Troquer, Y. and Thiébaux, J.P., 2008. Study of water tension differences in heterogeneous sandy soils using surface ERT. *Journal of Applied Geophysics*, *64*(3), pp.83-98.

Dirks, P.H. and Berger, L.R., 2013. Hominin-bearing caves and landscape dynamics in the Cradle of Humankind, South Africa. *Journal of African Earth Sciences*, *78*, pp.109-131.

Dirks, P.H., Placzek, C.J., Fink, D., Dosseto, A. and Roberts, E., 2016. Using 1 0 Be cosmogenic isotopes to estimate erosion rates and landscape changes during the Plio-Pleistocene in the Cradle of Humankind, South Africa. *Journal of Human Evolution*, *96*, pp.19-34.

Durand, J.F., 2012. The impact of gold mining on the Witwatersrand on the rivers and karst system of Gauteng and North West Province, South Africa. *Journal of African Earth Sciences*, *68*, pp.24-43.

Eriksson, P.G., Bartman, R., Catuneanu, O., Mazumder, R. and Lenhardt, N., 2012. A case study of microbial mat-related features in coastal epeiric sandstones from the Paleoproterozoic Pretoria Group (Transvaal Supergroup, Kaapvaal craton, South Africa); The effect of preservation (reflecting sequence stratigraphic models) on the relationship between mat features and inferred paleoenvironment. *Sedimentary Geology*, *263*, pp.67-75.

Ewusi, A 2006. Groundwater exploration and management using Geophysics: Northern Region of Ghana, Doctoral dissertation, Brandenburg Technical University of Cottbus, viewed 4 September 2016, < https://opus4.kobv.de/opus4-btu/files/26/Diss_Ewusi_neu.pdf >.

Fuchs, S., Schumann, D., Williams-Jones, A.E. and Vali, H., 2015. The growth and concentration of uranium and titanium minerals in hydrocarbons of the Carbon Leader Reef, Witwatersrand Supergroup, South Africa. *Chemical Geology*, *393*, pp.55-66.

Fuggle, R.F. and Rabie, M.A. eds., 1992. *Environmental Management in South Africa*. Juta & Company Limited.

Giampaolo, V., Capozzoli, L., Grimaldi, S. and Rizzo, E., 2016. Sinkhole risk assessment by ERT: The case study of Sirino Lake (Basilicata, Italy). *Geomorphology*, *253*, pp.1-9.

Giguère, R., Fradette, L., Mignon, D. and Tanguy, P.A., 2008. ERT algorithms for quantitative concentration measurement of multiphase flows. *Chemical Engineering Journal*, *141*(1), pp.305-317.

González-Álvarez, I., Ley-Cooper, A.Y. and Salama, W., 2016. A geological assessment of airborne electromagnetics for mineral exploration through deeply weathered profiles in the

southeast Yilgarn Cratonic margin, Western Australia. *Ore Geology Reviews*, *73*, pp.522-539.

Guy, B.M., Ono, S., Gutzmer, J., Kaufman, A.J., Lin, Y., Fogel, M.L. and Beukes, N.J., 2012. A multiple sulfur and organic carbon isotope record from non-conglomeratic sedimentary rocks of the Mesoarchean Witwatersrand Supergroup, South Africa. *Precambrian Research*, *216*, pp.208-231.

Hobbs, P.J., Butler, M., Coetzee, H., Jamison, A., Leyland, R. and Venter, J., 2011. Situation assessment of the surface water and groundwater resource environments in the Cradle of Humankind World Heritage Site. *Report prepared for the Management Authority. Pretoria: Economic Development Department*.

Hobbs, P.J., 2013. Pilot implementation of a surface water and groundwater resources monitoring programme for the Cradle of Humankind World Heritage Site. *Pretoria: Council for Scientific and Industrial Research Natural Resources & the Environment*.

Hobbs, P.J., 2014. Surface water and groundwater resources monitoring, Cradle of Humankind World Heritage Site, Water resources status report for the period April to September 2014. CSIR/NRE/WR/ER/2014/0063/A. Gauteng Province, South Africa.

Hobbs, P.J., 2015. Surface water and groundwater resources monitoring, Cradle of Humankind World Heritage Site, Water resources status report for the period April 2014 to March 2015. CSIR/NRE/WR/ER/2015/0026/A. Gauteng Province, South Africa.

Holland, M. and Witthüser, K.T., 2009. Geochemical characterization of karst groundwater in the cradle of humankind world heritage site, South Africa. *Environmental geology*, *57*(3), pp.513-524.

Ibeneme, S.I., Ibe, K.K., Selemo, A.O., Nwagbara, J.O., Obioha, Y.E., Echendu, K.O. and Ubechu, B.O., 2013. Geoelectrical Investigation of a Proposed Dam Site in a Sedimentary Terrain: Case Study of Aba River at Amapu-Ideobia, Akanu Ngwa Southeastern Nigeria. *International Journal of Geosciences*, *2013*.

Johnson, T.C., Slater, L.D., Ntarlagiannis, D., Day-Lewis, F.D. and Elwaseif, M., 2012. Monitoring groundwater-surface water interaction using time-series and time-frequency analysis of transient three-dimensional electrical resistivity changes. *Water Resources Research*, *48*(7).

Jones, G., Zielinski, M. and Sentenac, P., 2012. Mapping desiccation fissures using 3-D electrical resistivity tomography. *journal of Applied Geophysics*, *84*, pp.39-51.

Kemna, A 2000. Tomographic inversion of complex resistivity: Theory and application, Doctoral dissertation, Ruhr-University Bochum, viewed 10 March 2016, <https://www.geo.uni-bonn.de/mitarbeiter/Andreas-Kemna/dissertation>.

Klimchouk, A., 2009. Morphogenesis of hypogenic caves. *Geomorphology*, *106*(1), pp.100-117.

Kuras, O., Pritchard, J.D., Meldrum, P.I., Chambers, J.E., Wilkinson, P.B., Ogilvy, R.D. and Wealthall, G.P., 2009. Monitoring hydraulic processes with automated time-lapse electrical resistivity tomography (ALERT). *Comptes Rendus Geoscience*, *341*(10), pp.868-885.

Liu, Q., Han, Y. and Zhang, X., 2014. An image reconstruction algorithm based on Bayesian theorem for electrical resistance tomography. *Optik-International Journal for Light and Electron Optics*, *125*(20), pp.6090-6097.

Loke, M.H. and Barker, R.D., 1996. Rapid least-squares inversion of apparent resistivity pseudosections by a quasi-Newton method. *Geophysical prospecting*, *44*(1), pp.131-152.

Loke, M.H., Acworth, I. and Dahlin, T., 2003. A comparison of smooth and blocky inversion methods in 2D electrical imaging surveys. *Exploration Geophysics*, *34*(3), pp.182-187.

Loke, M.H., Chambers, J.E., Rucker, D.F., Kuras, O. and Wilkinson, P.B., 2013. Recent developments in the direct-current geoelectrical imaging method. *Journal of Applied Geophysics*, *95*, pp.135-156..

Mao, D., Revil, A., Hort, R.D., Munakata-Marr, J., Atekwana, E.A. and Kulessa, B., 2015. Resistivity and self-potential tomography applied to groundwater remediation and contaminant plumes: Sandbox and field experiments. *Journal of Hydrology*, *530*, pp.1-14.

Meschke, K., Herdegen, V., Aubel, T., Janneck, E. and Repke, J.U., 2015. Treatment of opencast lignite mining induced acid mine drainage (AMD) using a rotating microfiltration system. *Journal of Environmental Chemical Engineering*, *3*(4), pp.2848-2856.

Nguyen, F., Garambois, S., Jongmans, D., Pirard, E. and Loke, M.H., 2005. Image processing of 2D resistivity data for imaging faults. *Journal of Applied Geophysics*, *57*(4), pp.260-277.

Nordstrom, D.K., 2011. Hydrogeochemical processes governing the origin, transport and fate of major and trace elements from mine wastes and mineralized rock to surface waters. *Applied Geochemistry*, *26*(11), pp.1777-1791.

Nordstrom, D.K., Blowes, D.W. and Ptacek, C.J., 2015. Hydrogeochemistry and microbiology of mine drainage: An update. Applied Geochemistry, 57, pp.3-16.

Oberdörster, C 2010. Hydrological characterization of a forest soil using electrical resistivity tomography*,* Doctoral dissertation, The University of Bonn, viewed 15 July 2016, < http://hss.ulb.uni-bonn.de/2010/2210/2210.pdf>

Oberholster, P.J., Genthe, B., Hobbs, P., Cheng, P.H., De Klerk, A.R. and Botha, A.M., 2013. An ecotoxicological screening tool to prioritise acid mine drainage impacted streams for future restoration. *Environmental pollution*, *176*, pp.244-253.

Orlando, L., 2013. GPR to constrain ERT data inversion in cavity searching: Theoretical and practical applications in archeology. *Journal of Applied Geophysics*, *89*, pp.35-47.

Power, C., Gerhard, J.I., Karaoulis, M., Tsourlos, P. and Giannopoulos, A., 2014. Evaluating four-dimensional time-lapse electrical resistivity tomography for monitoring DNAPL source zone remediation. *Journal of contaminant hydrology*, *162*, pp.27-46..

Power, C., Gerhard, J.I., Tsourlos, P., Soupios, P., Simyrdanis, K. and Karaoulis, M., 2015. Improved time-lapse electrical resistivity tomography monitoring of dense non-aqueous phase liquids with surface-to-horizontal borehole arrays. *Journal of applied geophysics*, *112*, pp.1-13.

Robins, N.S., Chilton, P.J. and Cobbing, J.E., 2007. Adapting existing experience with aquifer vulnerability and groundwater protection for Africa. *Journal of African Earth Sciences*, *47*(1), pp.30-38.

Rucker, D., 2014. Investigating motion blur and temporal aliasing from time-lapse electrical resistivity. *Journal of Applied Geophysics*, *111*, pp.1-13.

Shaaban, F.F. and Shaaban, F.A., 2001. Use of two-dimensional electric resistivity and ground penetrating radar for archaeological prospecting at the ancient capital of Egypt. Journal of African Earth Sciences, 33(3), pp.661-671.

Simate, G.S. and Ndlovu, S., 2014. Acid mine drainage: Challenges and opportunities. *Journal of Environmental Chemical Engineering*, *2*(3), pp.1785-1803.

Tsourlos, P., Papadopoulos, N., Papazachos, C., Yi, M.J. and Kim, J.H., 2014. Efficient 2D inversion of long ERT sections. *Journal of Applied Geophysics*, *105*, pp.213-224.

Van Schoor, M 2009. Using electrical resistance tomography (ERT) and induced polarisation (IP) tomography to map potholes and iron-rich ultramafic pegmatite bodies in South African platinum mines, Doctoral dissertation, Lancaster University.

Van Zijl, J.S.V., 1977. *A practical manual on the resistivity method*. National Physical Research Laboratory, CSIR.

Viehmann, S., Bau, M., Smith, A.J., Beukes, N.J., Dantas, E.L. and Bühn, B., 2015. The reliability of~ 2.9 Ga old Witwatersrand banded iron formations (South Africa) as archives for Mesoarchean seawater: Evidence from REE and Nd isotope systematics. *Journal of African Earth Sciences*, *111*, pp.322-334.

Wagner, F.M., Möller, M., Schmidt-Hattenberger, C., Kempka, T. and Maurer, H., 2013. Monitoring freshwater salinization in analog transport models by time-lapse electrical resistivity tomography. *Journal of Applied Geophysics*, *89*, pp.84-95.

Wiwattanachang, N. and Giao, P.H., 2011. Monitoring crack development in fiber concrete beam by using electrical resistivity imaging. *Journal of Applied Geophysics*, *75*(2), pp.294-304.

Zeng, R.Q., Meng, X.M., Zhang, F.Y., Wang, S.Y., Cui, Z.J., Zhang, M.S., Zhang, Y. and Chen, G., 2016. Characterizing hydrological processes on loess slopes using electrical resistivity tomography–A case study of the Heifangtai Terrace, Northwest China. *Journal of Hydrology*, *541*, pp.742-753.